Petroleum Science 23 (2026) 1138–1158

Contents lists available at ScienceDirect

Petroleum Science

journal homepage: www.keaipublishing.com/en/journals/petroleum-science

Original Paper

The control of paleo-geomorphology on the depositional architecture of a Late Jurassic axial submarine fan, North Sea, UK

Ji-Tao Yu [a,b], Sheng-He Wu [a,b,*], Ming-Ming Qi [c], Zhen-Hua Xu [a,b], Shu-Chun Cao [c], Wei Du [a,b], Jing-Jing Li [a,b], Yu-Fei Zhang [d], Han Liu [a,b], Muhammad Ubaid Umar [a,b]

[a] College of Geosciences, China University of Petroleum (Beijing), Beijing, 102249, China
[b] State Key Laboratory of Petroleum Resources and Engineering, China University of Petroleum (Beijing), Beijing, 102249, China
[c] CNOOC International Limited, Beijing, 100028, China
[d] Research Institute, CNOOC China Limited, Hainan Branch, Haikou, 570311, Hainan, China

ARTICLE INFO

Article history:
Received 2 August 2025
Received in revised form
24 December 2025
Accepted 19 January 2026
Available online 23 January 2026

Edited by Xi Zhang and Jie Hao

Keywords:
Paleo-geomorphology
Depositional architecture
Axial submarine fan
Slope break
The North Sea

ABSTRACT

The depositional architecture of submarine fans in rift basins is significantly controlled by complex geomorphology created by widespread normal faults, presenting a key challenge in deep-water sedimentology. Although extensive previous studies have established depositional architectures and sand body distribution patterns of transverse submarine fans controlled by graben boundary faults and interbasin transfer zones, research on how axial submarine fan architecture responds to intra-graben slope gradients and evolving transverse confinement remains inadequate. This study takes the Upper Jurassic B4 oil group in the North Sea X Oilfield as an example. By using 3D seismic data, cores and logging data to restore paleo-geomorphology and dissect depositional architecture, and further reveal the controls of intra-graben paleo-geomorphic variations on axial submarine fan depositional architecture. Our analysis shows that the paleogeomorphology in the study area features axial stepped slope breaks and phased evolution in transverse confinement. As the axial slope transitions from extremely steep slope segments to steep slope segments, slope transition zones and gentle slope segments, turbidity currents evolve from supercritical to subcritical states through hydraulic jumps, while generating divergent flows. This progression drives architectural transformation from sediment bypass, incised channel–overbank systems, distributary channels and channelized lobes to lobes. Concurrently, phased transverse confinement evolution controls vertical stacking characteristics of individual channel–lobes: early asymmetric stages produce lateral migration stacking; middle symmetric stages develop unordered compensational stacking; and late locally confined stages form deflected retrogradational stacking. We propose a dynamic submarine fan depositional architecture response model, which emphasizes how evolving paleo-geomorphology directly controls spatiotemporal configurations of architectural elements by altering gravity flow pathways and energy distribution, and is further modified by feedbacks where the deposits themselves become influencing topographic elements. It provides a new perspective for deep-water depositional models and reservoir prediction in areas with similar geomorphic settings.

1. Introduction

Submarine fans, as important products of gravity flow sedimentation, have attracted attention due to their rich hydrocarbon resource potential (Mutti, 1977; Normark et al., 1998; Shanmugam, 2016). They are widely distributed across basins with diverse tectonic settings (Shanmugam and Moiola, 1988; Weimer and Link, 1991), including rift basins within divergent plate margins (Patruno et al., 2021; Tian et al., 2024), passive continental margin

* Corresponding author.
E-mail address: reser@cup.edu.cn (S.-H. Wu).
Peer review under the responsibility of China University of Petroleum (Beijing).

https://doi.org/10.1016/j.petsci.2026.01.030

basins (Chen et al., 2024a, 2024b; Zhang et al., 2016), forearc basins (Higley, 2004) and foreland basins (Bell et al., 2018; Moody et al., 2012). Among these, rift basin-type submarine fans exhibit extremely complex sedimentary characteristics due to the influence of widely distributed normal faults, making them a hotspot in deep-water sedimentation research (Gawthorpe et al., 1993; Gupta et al., 1999; Nyíri et al., 2021; Steventon et al., 2021).

Within rift basins, gravity flow deposits can be transported along fault strikes to form axial submarine fans or perpendicular to fault strikes to form transverse submarine fans (Henstra et al., 2017; Leeder and Gawthorpe, 1987). Previous studies have focused on the impact of graben boundary faults on the sedimentary characteristics of rift basin-type submarine fans. Under the influence of these faults, axial submarine fans transport along the strike of graben boundary faults toward low-lying areas of slopes, typically exhibiting extensive sand body distribution, large-scale features, vertical aggradation or compensational stacking within the fan, and good sand body connectivity (Prosser, 1993; Steventon et al., 2021; Taylor et al., 2020; Tian et al., 2024). In contrast, transverse submarine fans transport along fault dip directions toward topographic lows, with shorter sand body extensions, smaller scales, predominantly vertical aggradation or retrogradational stacking within the fan, and isolated geometries between individual fans on the plane (Gawthorpe and Leeder, 2000; McArthur et al., 2016; Privat et al., 2024; Prosser, 1993; Ravnas and Steel, 1998; Sharp et al., 2000). However, localized topographic variations within grabens or half-grabens (i.e., intra-graben features such as slope gradient change and growth faults) can alter the direction and fluid state of gravity flow (Ge et al., 2018; Kneller, 1995; Postma and Cartigny, 2014), that directly control the evolution and stacking patterns of submarine fan sedimentation. In comparison with the role of large-scale graben boundary faults, the intra-graben paleo-geomorphology has not been adequately studied. Although recent studies on transverse submarine fan systems within the Heather and Draupne formations of the North Sea Viking Graben have emphasized the role of closely spaced fault terraces within half-grabens (Jackson et al., 2011; Tillmans et al., 2021). These studies indicated that the transfer zones between closely spaced fault terraces can alter local transport routes of channelized lobes, the footwalls of faults can act as major stacking zones of channelized lobes with thick sand bodies and patchy geometries rather than lobate-like. But to date, there remains no documented research on how intra-graben paleo-geomorphological variations in slope gradient and confinement control the depositional architecture of axial submarine fans in rift basins.

The Moray Forth Basin in the North Sea, UK, experienced syn-rift phases during the Mesozoic (Cowie et al., 2005; Underhill and Richardson, 2022). In this paper, taking the axial submarine fan deposits in the Upper Jurassic rift setting of the X oil field in the Moray Forth Basin (McKinnon, 2013; Taylor et al., 2020) as an example, we comprehensively applied data from cores, well logs, and 3D seismic data to elucidate the controlling mechanisms of intra-graben paleo-geomorphology on axial submarine fan architecture, and further establish corresponding depositional models. This work enhances the theoretical framework of rift basin axial fan depositional architecture under paleo-geomorphic controls and provides guidance for refined reservoir prediction in similar hydrocarbon fields.

2. Geological setting

The Moray Forth Basin, situated in the Central North Sea area, represents a significant component of the Mesozoic triple-rift system in the North Sea (Coward et al., 2003). During the Late Jurassic syn-rift period, the Moray Forth Basin developed numerous NE–SW and NW–SE trending normal faults following two distinct phases of rift extension (Erratt et al., 1999; Patruno et al., 2021). The study area is located within the Buchan Graben on the slope zone of the Moray Forth Basin, covering approximately 111 km^2 in an offshore region situated about 50 km from the Scottish mainland (Ray et al., 2010) (Fig. 1(a)). Two approximately E–W trending confined graben boundary faults flank the northern and southern margins of the study area, while the graben interior contains multiple growth faults and a complex fault system (Dore and Robbins, 2005; Ray et al., 2010; Taylor et al., 2020) (Fig. 1(b)).

The Upper Jurassic reservoirs in the study area are primarily composed of the BZ Sandstone Member within the lower Kimmeridge Clay Formation (Guariguata-Rojas and Underhill, 2017) (Figs. 1(c) and 2), which is subdivided into five oil groups (B0, B1, B2, B3, B4) from its base to the top (Ray et al., 2010), corresponding to third-order genetic sequences J62-J66 (Copestake and Partington, 2023; Partington et al., 1993) (Fig. 2). Previous studies indicate that during the deposition of the BZ Sandstone Member, deltaic and shallow-marine sandy sediments sourced from the Grampian Spur in the southwest were transported via gravity flows along the slope into the study area (Fig. 1(a)), forming typical deep-water axial channel–lobe systems in the study area (Patruno et al., 2021; Underhill, 1998; Fraser et al., 2003). The target interval of this study is the B4 oil group, which was deposited during a syn-kinematic setting. This period was also characterized by relatively low sea level, arid climatic conditions in the provenance area, and strong erosion (Hesselbo, 2008; Hesselbo et al., 2009) (Fig. 2). The sand-rich sediment supply delivered by event floods resulted in a very high net-to-gross ratio throughout the B4 oil group. Within the B4 oil group, we hierarchically subdivided it into three sand groups (corresponding to channel–lobe systems), five sub-zones (corresponding to channel–lobe complex sets) and eleven single zones (corresponding to channel–lobe complexes) (Fig. 3). Each channel–lobe complex within a single zone may contain several individual channel–lobes.

Overall, the submarine fan within the target interval of the study area is composed of architectural elements including channel, overbank, and lobe. Sediment bypass occurs in the up-dip direction of the western study area, with sand bodies primarily deposited in the central and eastern regions (McKinnon, 2013; Taylor et al., 2020). The lithology of sand bodies is dominated by medium-fine sandstone with good sorting and low clay content. Weakly compacted reservoirs exhibit superior physical properties, showing an average porosity of approximately 24% and average permeability around 1600 mD, with some reservoir intervals demonstrating permeability exceeding 10,000 mD.

3. Data and methods

3.1. Data

This study utilized a comprehensive dataset comprising core samples, well logs, and seismic data. A total of 74 wells penetrates the target interval within the study area, with an average well spacing of approximately 1000 m (due to confidentiality concerns, well locations and well names have been partially displayed and modified, and all well depths have been converted to a normalized depth scale starting from 0 at the top of the target interval. The original absolute depths are not disclosed. All wells possess standard suite well log data, including gamma ray (GR), acoustic interval transit time (AC), density (DEN), resistivity (RT), neutron porosity (NEUTRON) and so on. Furthermore, core samples totaling approximately 3583 ft were acquired from the target interval in 12

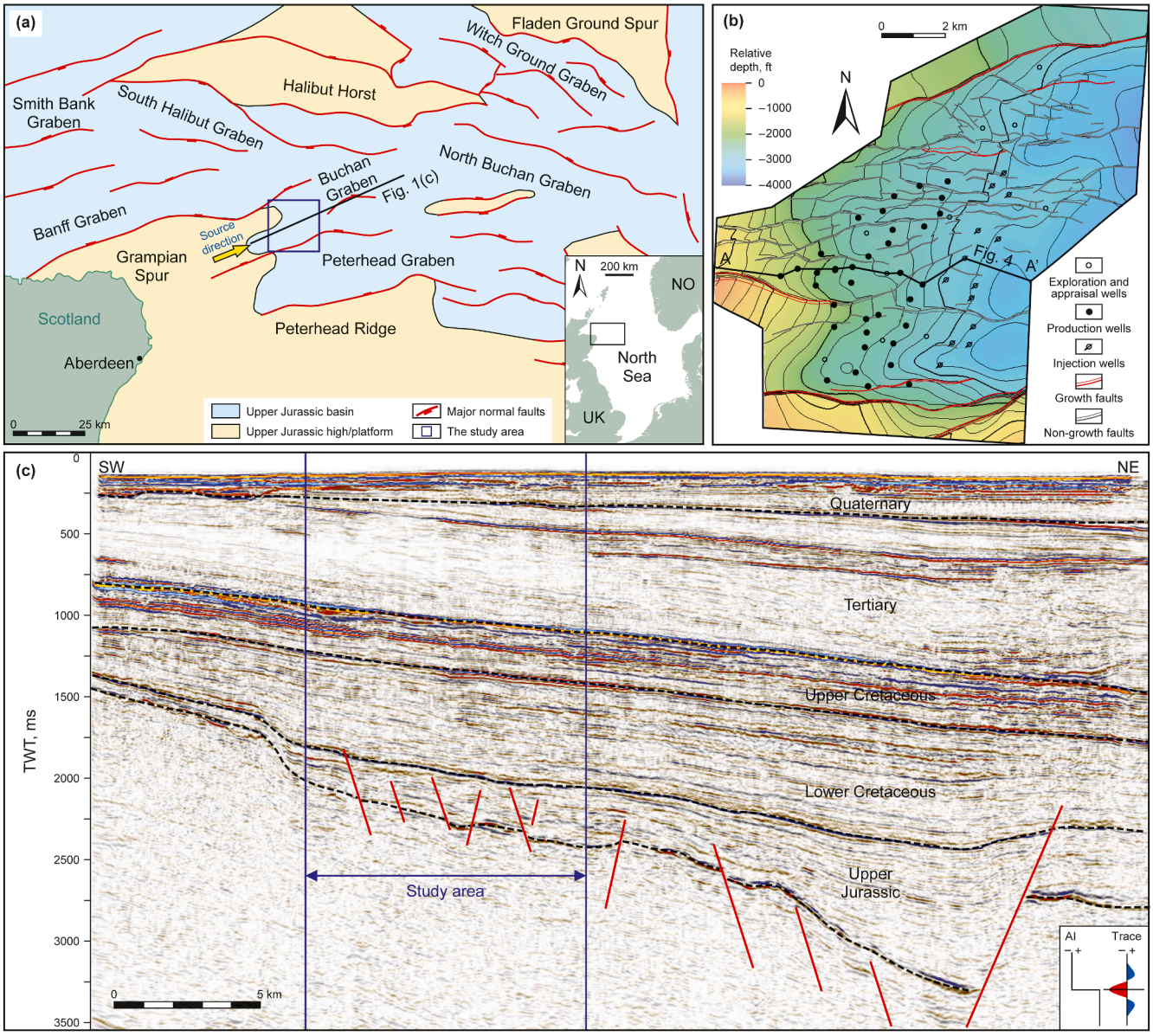

Fig. 1. Geological overview maps of the study area. (**a**) Map showing the regional structural framework of the Upper Jurassic in the Moray Forth Basin, North Sea, UK. The tectonic location of the study area is highlighted with a dark blue frame (modified after Ray et al., 2010). (**b**) Target interval top structure map showing the fault type, well location, and the study area boundary which also defines the seismic data extent (For confidentiality reasons, the structural map uses relative elevation depth, and only some of the well locations have been displayed). (**c**) Seismic profile and interpretation showing location of the study area, main faults and stratigraphic distribution characteristics. See Fig. 1(a) for the location of the cross-section (modified after Taylor et al., 2020). TWT = two-way time.

of these wells. High-resolution photographs of cores were taken to facilitate detailed observation. The seismic data, covering the entire study area, reveals that the Upper Jurassic target interval exhibits a bandwidth of 3–70 Hz with a dominant frequency of 31.5 Hz, yielding a vertical resolution of approximately 70 ft. The post-stack 3D seismic volume is displayed with negative polarity (SEG standard). Consequently, on the seismic profiles presented in this paper, an increase in acoustic impedance is characterized by a red (trough) reflection.

3.2. Methods

3.2.1. Paleo-geomorphological restoration

During the deposition period of the target interval, the study area remained in a deep-water disequilibrium continental slope environment. Erosion was absent, and terrigenous clastic sediment supply was abundant, resulting in an overfilled sedimentary state. Furthermore, considering the abundance of seismic and well log data available within the study area, the impression method was applied for quantitative paleo-geomorphological restoration (Jin et al., 2017; Lyu et al., 2022; Tang et al., 2023; Yu et al., 2022). The specific steps including (Jiang, 2018).

i) Selection of target horizons and an isochronous datum: Detailed seismic structural and horizon interpretation was conducted through well-to-seismic calibration. Within the target interval, three seismic horizons corresponding to the base of the LB4, MB4, and UB4 sand groups were tracked (Fig. 4), serving as the target horizons for paleo-geomorphological restoration. Above the target interval,

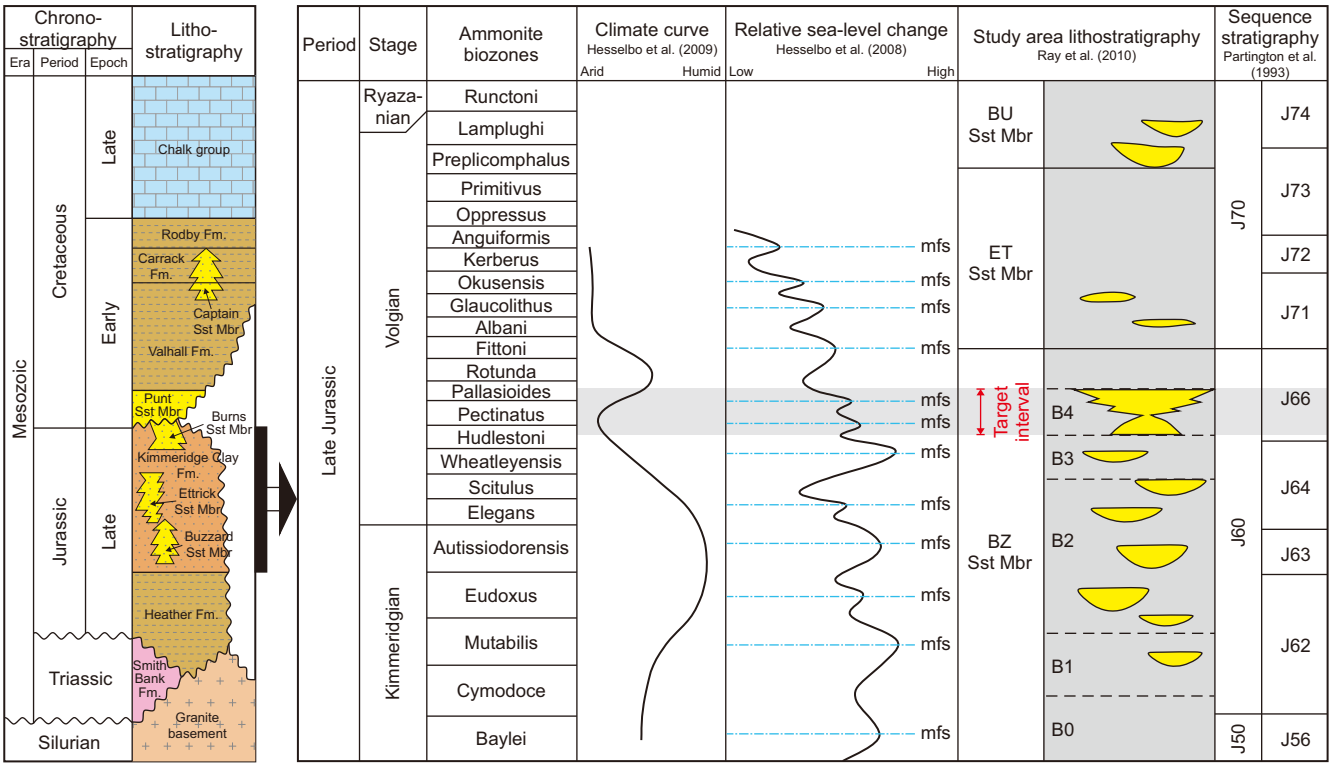

Fig. 2. Stratigraphic columns for the study area illustrating the regional lithostratigraphy (Ray et al., 2010), biostratigraphic zonation scheme (Partington et al., 1993), climate curve (Hesselbo et al., 2009), relative sea-level changes (Hesselbo, 2008), and sequence stratigraphy (Partington et al., 1993). (Modified after Taylor et al., 2020). The wavy lines represent regional unconformities, and the grey-shaded area is the target interval. Fm. = formation; mfs = maximum flooding surface; Sst = sandstone; Mbr = member.

the seismic event representing the base surface of J72 sequence was identified (Fig. 4). No unconformity exists between this surface and the underlying target interval, and the thickness of the overlying strata exhibits minimal variation. This indicates relatively subdued topography during the depositional period of this surface, qualifying it as an isochronous datum.

ii) Compaction correction: To restore the original sediment thickness, we applied compaction corrections accounting for lithology-dependent compaction. The depth-porosity relationship for each major lithology (shale, sandstone, carbonate) follows an exponential decay function Eq. (1):

$$\varphi_{(z)} = \varphi_0 e^{(-c*z)} \tag{1}$$

where $\varphi_{(z)}$ is porosity at burial depth, %; z is burial depth, km; φ_0 is initial depositional porosity, %; c denotes the compaction coefficient, fraction. The parameters φ_0 and c were adopted from the well-established North Sea basin models of Sclater and Christie (1980) for lithological consistency: shale: φ_0 = 63%, c = 0.51, sandstone: φ_0 = 49%, c = 0.27, carbonate (chalk): φ_0 = 70%, c = 0.71. These values were integrated with our well log-derived lithology proportions maps to apply lateral variable decompaction across the study area.

The study area has complex lithological combinations, and the overall restored thickness of the strata is expressed as Eq. (2) (Liu et al., 2025):

$$H = \sum_{i=1}^{n} h_i = \sum_{i=1}^{n} \left(1 - \varphi_{(z)i}\right) \times \frac{h_{0i}}{(1 - \varphi_{0i})} \tag{2}$$

where H is the restored thickness of the whole stratum, m; i = 1, 2, 3 … n, represents the number of single lithology layers, fraction; h_i is the restored thickness for a single lithology layer, m; h_0 is the present thickness of a particular lithology, m; $\varphi_{(z)i}$ is the porosity at burial depth z for a single lithology layer, %; φ_{0i} is initial depositional porosity for a single lithology layer, %. By summing the restored thickness of each layer, it is possible to calculate the restored thickness of the whole stratum.

iii) Growth fault correction: Given the presence of growth faults within the study area, 94 approximately east-west striking normal faults were identified using variance attribute analysis. Based on the ratio of stratigraphic thickness between opposing fault blocks, 6 growth faults were recognized (Fig. 1(b)), and their respective growth indices were determined. The hanging-wall restored thicknesses were corrected based on growth index of growth faults, effectively removing the syn-depositional tectonic thickening.

Following these corrections, the relative paleo-geomorphology prior to the deposition of each sand group was restored. From these surfaces, slope gradients were quantified by extracting topographic profiles along the source direction and calculating the average gradient over specific segments.

3.2.2. Depositional architecture dissection

The high-resolution isochronal stratigraphic framework, which serves as the foundation for the subsequent architectural analysis, was established through a method of “well-seismic integration, hierarchical constraint, model guidance, and dynamic-static combination”. Specifically, sand-group level correlations were

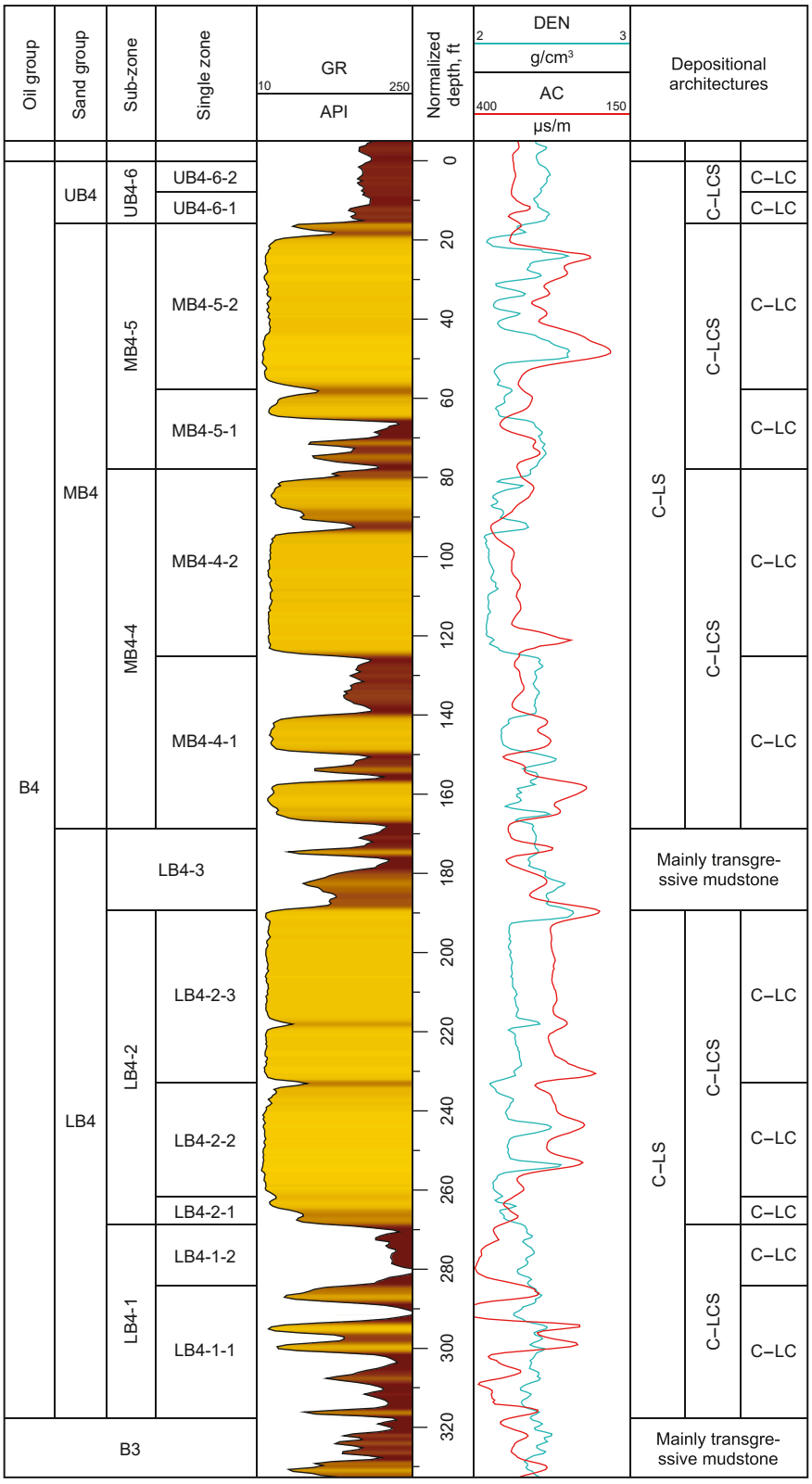

Fig. 3. Hierarchical isochronous stratigraphic division within the target interval of exploration well P1A and their corresponding different hierarchical depositional architectures (see Fig. 10 for well location). GR = gamma ray; DEN = density; AC = acoustic interval transit time; C–LS = channel–lobe system; C–LCS = channel–lobe complex set; C–LC = channel–lobe complex.

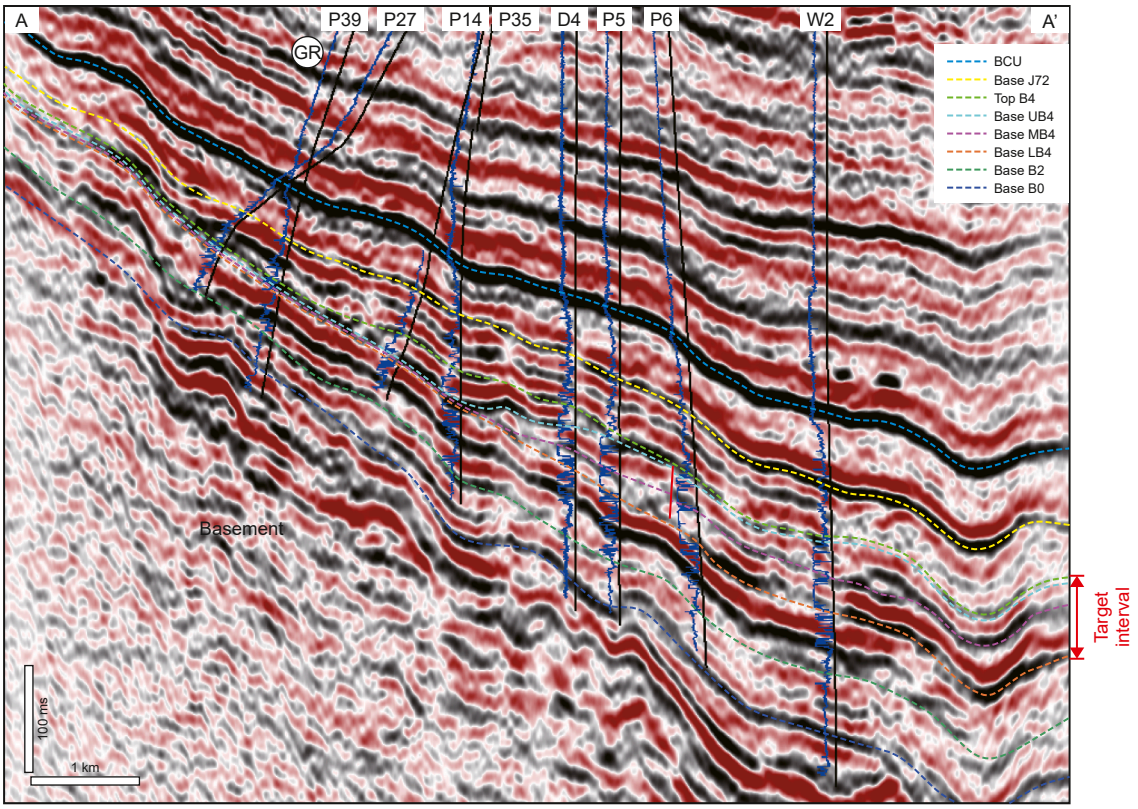

Fig. 4. Approximately west-east oriented seismic profile illustrating the target horizons (Base LB4, Base MB4 and Base UB4) and isochronous datum (Base J72 sequence) employed for paleo-geomorphological restoration. BCU= Base Cretaceous Unconformity. Section locations are shown in Fig. 1(b).

first constructed using well-seismic integration. Within this framework, sub-zone and single zone-level divisions were further refined based on the identification of laterally continuous mudstone separators, assisted by chemostratigraphic data and production dynamic data where available. The retrogradational stacking pattern provided additional chronostratigraphic constraints (Fig. 4). This framework was validated through multiple cross-well section correlations to ensure accuracy and lateral consistency.

Based on this high-resolution stratigraphic framework, the object of this architecture dissection is the individual channel–lobe within each single zone channel–lobe complex. However, constrained by the low dominant frequency of seismic data and complex fault development in the study area, the direct application of conventional seismic attributes (such as RMS amplitude or attribute fusion) for analyzing the internal architecture of submarine fans is not feasible. To fully exploit well and seismic information, this study first employs a frequency division inversion method based on a fine isochronal stratigraphic framework to predict sand body distribution, so as to clarify the architecture distribution characteristics of channel–lobe complexes. Subsequently, the lateral boundaries of individual channel–lobe are identified based on lateral thickness variations within the channel–lobe complexes. This approach enables architecture dissection at the scale of individual channel–lobe. The specific methods are as follows.

(1) Prediction of sand body distribution in single zone channel–lobe complexes

Sand body distribution prediction was conducted utilizing frequency division inversion, constrained by the single zone isochronous stratigraphic framework. The study area exhibits considerable complexity in lithotypes. Sandstones include loose high-porosity sandstones, uncemented sandstones, and calcite cemented sandstones. Argillaceous rocks comprise mudstones and mudstones interbedded with thin layers of cemented sandstone. Although the GR log effectively distinguishes between sandstone and argillaceous rock, correlation analysis between acoustic impedance (AI) data and GR log values reveals a poor relationship. Specifically, this is an overlapping range of GR and AI values between uncemented sandstones and mudstones, making it challenging to effectively identify sandstone solely through inversion of the GR log. However, the DEN log demonstrates effective discrimination between loose high-porosity sandstones, uncemented sandstones, and calcite cemented sandstones. Therefore, to integrate the strengths of both logs, a lithology curve (Lithlog) was constructed. Its expression is as follows:

$$\text{Lithlog} = \left(\frac{\text{GR}}{\text{GR}_{\text{max}}}\right) \times \left(1 - \frac{\text{DEN}}{\text{DEN}_{\text{max}}}\right) \quad (3)$$

where GR denotes the Gamma ray log value, API; GR_{max} is the maximum GR log value at the shale baseline, assigned a value of 300 API, DEN denotes the Density log, g/cm^3; DEN_{max} is the maximum DEN log value for calcite cemented sandstone, assigned a value of 3 g/cm^3.

Analysis of Lithlog alongside well-derived AI data demonstrates that distinct lithotypes generally correspond to distinct intervals of AI values (Fig. 5(a)). Thus, Lithlog can be employed as the inversion curve to effectively identify sandstones.

Secondly, although the seismic data within the study area exhibits a relatively low dominant frequency, it possesses a considerable effective bandwidth (3–70 Hz). Exploiting seismic information across different frequency bands, particularly higher

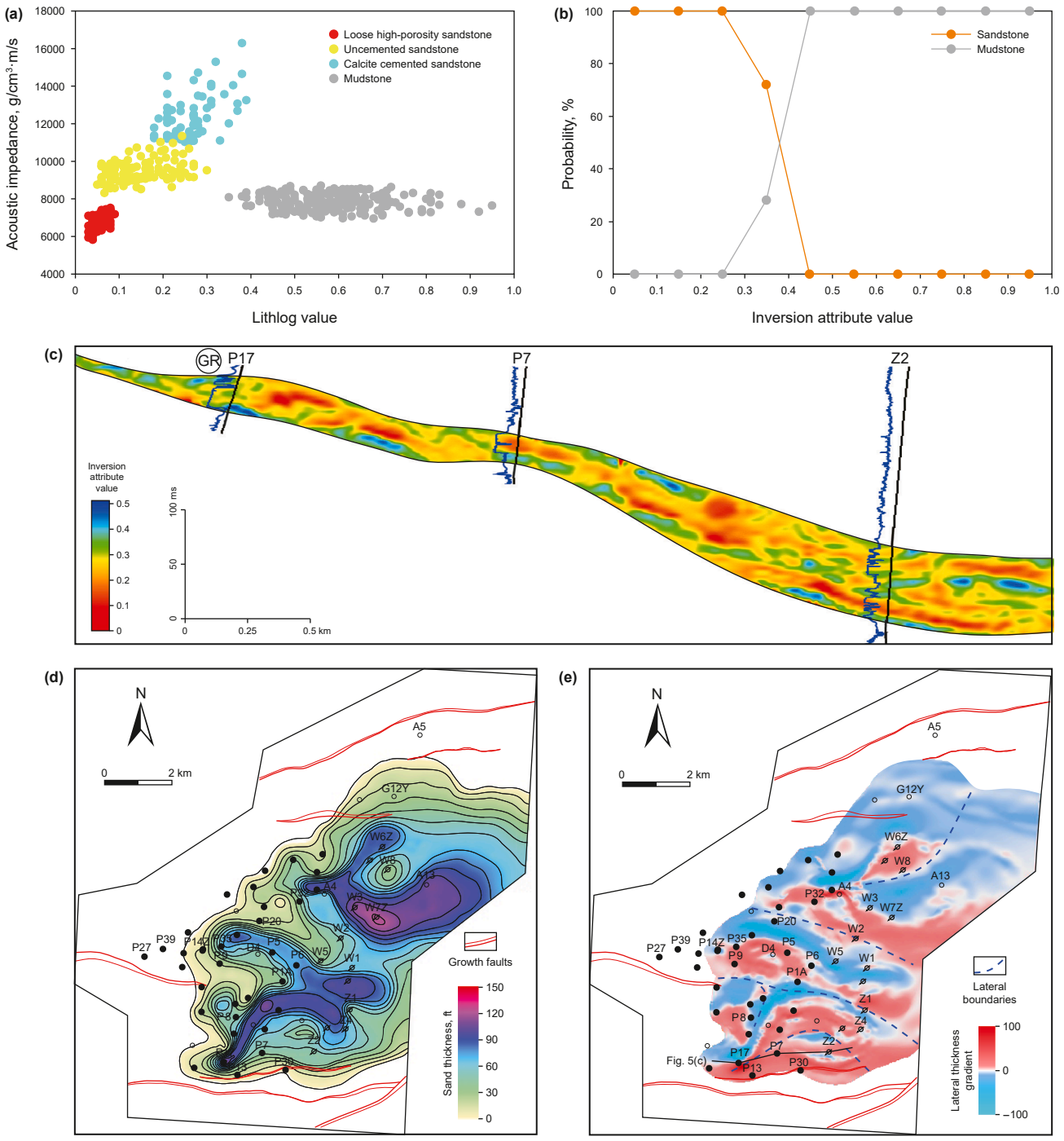

Fig. 5. (**a**) Cross spots of Lithlog values versus acoustic impedance values for different lithologies, showing distinct AI intervals. (**b**) Probability distribution curves of inversion attribute values versus occurrence probability for sandstone and mudstone, illustrating that sandstone probability rises with decreasing inversion attribute values below 0.45 and approaches 100% when the values are less than 0.25. (**c**) Cross-well seismic inversion profile of target interval (profile location shown in Fig. 5(e)), where decreases in inverted attribute values (arrows) indicate sandstone thinning and the presence of lateral boundaries. (**d**) Sand thickness distribution map of a single zone (MB4-4-2) derived from the three-dimensional sand-shale model. (**e**) Lateral thickness gradient map of the single zone MB4-4-2.

frequencies, is essential for predicting sand body distribution within channel–lobe complexes. Frequency division inversion represents an effective methodology for this purpose (Li et al., 2019). Three optimal frequency volumes at 15, 35, and 70 Hz were selected for predicting relatively thick sand bodies (about 140 ft), moderately thick sand bodies (about 60 ft), and relatively thin sand bodies (about 30 ft), respectively. Then, an intelligent algorithm based on Support Vector Regression (SVR) was employed to construct a predictive model relating the Lithlog curve to well-side seismic traces within these three frequency bands, thereby enabling seismic frequency divided inversion. By extracting inversion attribute values from well-side traces and conducting probabilistic statistical analysis against actual lithotypes, the results reveal that the inversion volume exhibits

favorable sandstone identification performance. When the inverted attribute value falls below 0.25, the probability of sandstone reaches 100% (Fig. 5(b)).

Finally, building upon the seismic frequency division inversion results (Fig. 5(c)) and fully using well information, sand body distribution within channel–lobe complexes was predicted. A three-dimensional stratigraphic-structural model was constructed through well-seismic integration, constrained by the single zone isochronous stratigraphic framework and fault interpretation results. Employing the Cokriging algorithm, with interpreted sand body data from individual wells as hard data and the seismic inversion volume as soft data, a three-dimensional sand-shale model reflecting the spatial distribution of sand bodies was generated. This model subsequently enabled the extraction of sand thickness distribution maps for the channel–lobe complexes within the study area (Fig. 5(d)).

(2) Identification of individual channel–lobe

Individual channel–lobe typically exhibit a depositional morphology characterized by thicker centers and thinner margins. The lateral amalgamation of successive individual channel–lobe within a complex result in a lateral thickness pattern of "thick–thin–thick" in the composite sand body (Fig. 5(d)). By using this characteristic, the lateral boundaries of individual channel–lobe were delineated on the basis of the predicted sand body distribution map of the channel–lobe complex. This involved detecting lateral variations in thickness difference across inter-well facies transition zones using a specific parameter, the lateral thickness gradient (G). This parameter is defined as the derivative of sand body thickness taken perpendicular to the dominant source direction, expressed as Eq. (4):

$$G_{i,j} = \frac{\left(h_{j+1} - h_{j-1}\right)}{2\Delta y} \tag{4}$$

where $G_{i,j}$ denotes the lateral thickness gradient at grid cell (i,j), fraction; h denotes the sand body thickness, ft; y denotes distance along cross-source direction, m; Δy denotes grid cell size in y-direction, m; Subscripts $j-1$, j, $j+1$ denotes adjacent grid cells along y direction, fraction.

The sign of $G_{i,j}$ provides diagnostic insights into depositional positioning, when $G_{i,j} > 0$ indicates southward thinning of the sand body, signifying a location within the northern individual channel–lobe. $G_{i,j} < 0$ indicates northward thinning of the sand body, signifying a location within the southern individual channel–lobe. $G_{i,j} = 0$ correspond to local thickness minima, interpreted as lateral boundaries between adjacent individual channel–lobes.

Based on the zero-value distribution of $G_{i,j}$ and integrated with dynamic data, the lateral boundaries of individual channel–lobes were identified (Fig. 5(e)). Building upon the identified lateral boundaries of individual channel–lobes, lithofacies types and characteristics in the study area were investigated through systematic observation and description of abundant core data (including lithology and sedimentary structures). Architectural elements were further identified by integrating these findings with characteristic well-log responses. Concurrently, multi-well cross-section analysis was employed to examine the stack relationships of individual channel–lobes.

On this basis, quantitative scale of individual channels and lobes were measured and calculated. The specific parameters and their definitions are as follows. Bifurcation angle between distributary channels: the angle between the axial trends of two distributary channels at their point of divergence. Average width of individual channels or lobes: the mean value of widths measured at different planar positions perpendicular to the element's axis. Average thickness of individual channels or lobes: the mean value of thicknesses measured at different vertical positions. Maximum length of individual channels or lobes: the longest straight-line distance of an individual channel or lobe parallel to the source direction. Maximum width of individual channels or lobes: the greatest straight-line distance of an individual channel or lobe perpendicular to the source direction.

4. Results

The development of Upper Jurassic channel–lobe systems in the study area was preconditioned by active rifting, which created complex fault-bounded topography and provided ample accommodation space. This was complemented by sustained sediment supply, from the Grampian Spur, enabling the construction of extensive submarine fans (Patruno et al., 2021; Ray et al., 2010; Underhill, 1998). The following sections detail the paleo-geomorphology that guided these systems and characterize their internal architecture.

4.1. Paleo-geomorphological characteristics and evolution of the study area

4.1.1. LB4 sand group

During the deposition of the LB4 sand group, the study area was situated within a confined graben of the continental slope. Significant paleo-geomorphic variations were observed across different orientations. Axially, the study area was characterized by stepped slope breaks, defined as zones of abrupt gradient decrease downslope (steep-to-gentle) (Pohl et al., 2020; Wang et al., 2002). The primary slope break developed approximately 500 m beyond the western boundary of the study area, with its upper slope forming a steep slope environment. Although seismic data for this specific region were not acquired in this study, the slope gradient of the upper slope was estimated at approximately 7.5° based on the gradient ratio between this region and the study area from previous seismic profiles (Fig. 1(c)) (Taylor et al., 2020). The study area as a whole resided on the lower slope of the east-dipping primary slope break, where two secondary slope breaks were further developed.

The secondary slope break zone 1 (SSBZ1) occurred in the central part of the study area (Fig. 6). Axially, the slope gradient decreased rapidly from approximately 3.2° to about 0.4° across this slope break zone (Fig. 7(a)). The width of SSBZ1 is about 0.15 km, with the upper slope of the SSBZ1 extending about 0.5 km axially, while the axial length of the lower slope is approximately 1 km. Immediately east of the SSBZ1, the secondary slope break zone 2 (SSBZ2) is developed, with the axial slope gradient decreasing abruptly from approximately 2.8° to about 0.5°. The width of SSBZ2 is about 0.2 km, with the upper and lower slopes of the SSBZ2 both measuring roughly 2 km in axial length (Fig. 7(a)).

Transversely, the study area is bounded by growth faults F1-1, F1-2, and F6 on its northern and southern margins, forming a graben structure (Figs. 6 and 7(b)). These boundary faults exhibit a throw of more than 600 ft. Under their strong confining influence, the paleo-geomorphology manifested as a distinct graben. This graben displays lateral asymmetry, characterized by a lower and steeper southern topography with a transverse slope gradient of approximately 4.3° and a higher and gentler northern topography with a transverse slope gradient of about 0.7°, forming a narrow strip-shaped trough nearly 4 km wide in the southern study area. Within the graben, four growth faults were further developed,

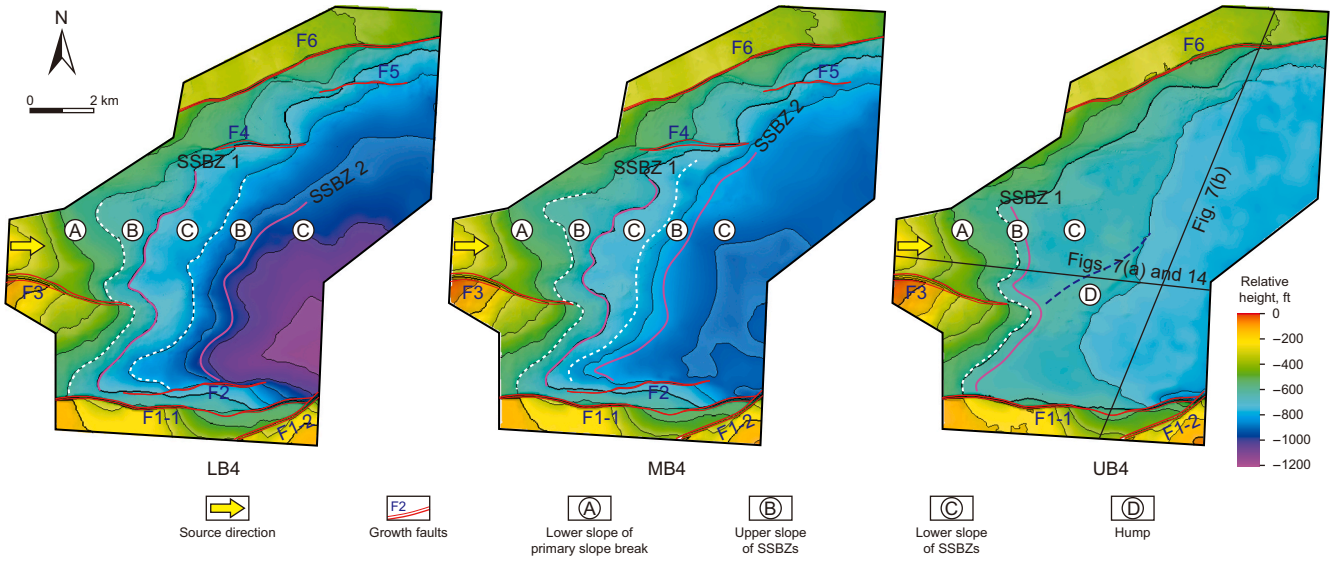

Fig. 6. Paleo-geomorphology prior to deposition of each sand group, from bottom to top being the LB4, MB4, and UB4 sand groups. The thicker purple line denotes the location of the SSBZs, and the thinner white dashed line indicates the boundary between the upper and lower slopes.

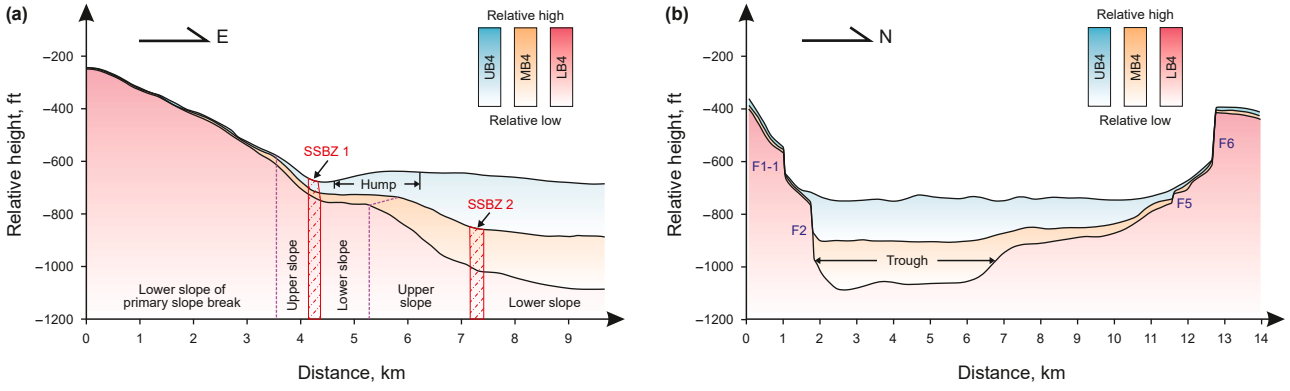

Fig. 7. Paleo-geomorphic characteristics and evolution prior to deposition of each sand group along-source direction (nearly W-E trending) (**a**) and cross-source direction (nearly S-N trending) (**b**). The boxes hatched with red diagonal dashed lines denote the corresponding secondary slope break zones (SSBZs), where the slope gradient changes from steep to gentle down-dip. The width of the boxes approximately corresponds to the width of the slope break zones. Section locations are shown in Fig. 6.

though their throws were relatively smaller than those of the graben boundary faults, generally around 50 ft. Only the eastern segment of fault F2 and the western segment of fault F3 had throws exceeding 100 ft, exerting notable lateral confinement at these high-throw sections (Fig. 7(b)).

4.1.2. MB4 sand group

During the deposition of the MB4 sand group, the paleo-geomorphology of the study area developed inheriting characteristics from the previous period (Fig. 6), influenced by the infilling and leveling effects of the LB4 sand group. Axially, the SSBZ1and SSBZ2 morphologies persisted, though the gradient of each slope break zone decreased compared to the prior depositional stage (Fig. 7(a)). In the central study area, within the SSBZ1 (width about 0.1 km), the axial slope gradient decreased rapidly from approximately 3.3° to about 0.1°, with the upper slope extending approximately 0.5 km axially and the lower slope about 1 km. SSBZ2 (width about 0.2 km) featured an abrupt axial slope gradient reduction from approximately 1.3° to about 0.4°, where the upper slope measures approximately 1.5 km, and the lower slope 2 km in axial length (Fig. 7(a)).

Transversely, the asymmetry of the paleo-geomorphology was diminished, manifested as a southern transverse slope of approximately 3° and a northern transverse slope of about 0.5°. The throws of both the graben boundary faults and internal growth faults remained consistent with those of the previous period, continuing to exert lateral confinement effects (Figs. 6 and 7(b)).

4.1.3. UB4 sand group

During the deposition of the UB4 sand group, further influenced by the infilling and leveling effects of the MB4 sand group, the paleo-geomorphology of the study area showed significant differences from the previous period (Fig. 6).

Axially, the SSBZ2 morphology was largely infilled, leaving only the SSBZ1 (Fig. 6). Furthermore, an approximately 2 km long and 50 ft high hump developed within the eastern of this SSBZ1. In the central study area, the SSBZ1 (width about 0.1 km) featured an upper slope with an axial slope gradient of approximately 2° and axial length of about 0.5 km, while its lower slope (including the hump) shows an axial slope gradient of about 0.3° and extends about 5 km (Fig. 7(a)).

Transversely, the geomorphology of the study area transformed into a symmetrical graben. Except for the graben boundary faults F1-1, F1-2, F6 and the internal fault F3, which continued to exert lateral confinement, all other growth faults were filled in and no longer exerted confining effects (Figs. 6 and 7(b)).

4.2. Architectural characteristics of the submarine fan in the study area

4.2.1. Types and characteristics of architectural elements

Submarine fan depositional processes are highly complex, involving transformations in fluid type within gravity flows during transport (Bouma, 1962; Lowe, 1982; Shanmugam, 1996, 1997; Shanmugam et al., 1985; Zhang et al., 2015). Consequently, significant variations exist in lithofacies types and morphological features among distinct architectural elements, leading to corresponding differences in well-log response characteristics and the planar distribution of sand bodies (Zhang et al., 2016). Through systematic core observation and description, eleven lithofacies types were classified in the submarine fan of the study area (Fig. 8). Based on the combinatorial characteristics of these lithofacies, well-log responses, and the planar geometry of sand bodies, three principal architectural elements (channel, overbank, and lobe) along with hemipelagic mudstone were identified within the submarine fan. The defining characteristics of each architectural element were subsequently determined (Fig. 9).

(1) Channel

Description. The lithofacies association exhibits a typical fining-upward succession (Fig. 9(a)). From base to top, it is predominantly characterized by thick-bedded (up to more than 30 ft) massive very coarse sandstone, massive coarse sandstone, normal grading medium-coarse sandstone, and parallel-bedded fine sandstone (Fig. 8(a)–(c) and (g)). Locally developed at the base are massive very coarse or coarse sandstone with mud clasts or erosional surface (Fig. 8(b)). On the density log, this succession displays a bell shape with a deflection potentially developing at the base (Fig. 9(a)).

Interpretation. Channels serve as the primary pathways for gravity flow transportation and deposition. Erosional structures at the base, which may include irregular mud clasts, indicate significant erosive capacity during gravity flow transport (Allen, 1982; Li et al., 2017; Normark, 1970). Massive very coarse sandstone or normal grading medium-coarse sandstone is deposited above the erosional structures, where the latter corresponds to the Ta division of the Bouma sequence (Bouma, 1962). Given the high frequency of normal grading within the basal coarse sandstones in cored intervals, coupled with thin-section observations revealing moderately to well-sorted sandstones with low matrix content (typically less than 3%), these deposits are interpreted as high-density turbidity current deposits, as defined by Lowe (1982). The Ta divisions observed in core, characterized by erosional bases and upward development of structureless coarse-tail graded sediments deposited (Fig. 9(a)), indicate hindered settling in high-density turbidity currents potentially triggered by hydraulic jumps (Postma et al., 2009). Furthermore, the parallel-bedded fine sandstone at the top corresponds to the Tb division of the Bouma sequence, signifying waning flow energy during the terminal phase of channel filling (McHargue et al., 2011; Tian et al., 2023). The successions of these facies, specifically the top-cut-out Bouma sequences composed of Ta to Tb divisions from base to top (Fig. 9(a)), can be interpreted as typical supercritical turbidity current deposits formed down the lee face of cyclic steps (Postma and Cartigny, 2014; Postma et al., 2014; Ventra et al., 2015), although the core scale often captures individual depositional units rather than the full bedform set.

(2) Overbank

Description. The lithofacies association is dominated by horizontal-bedded mudstone (Fig. 8(l)) interbedded with thin (typically less than 4 ft) layers of massive fine sandstone, massive very fine sandstone, parallel-bedded very fine sandstone, or cross-bedded very fine sandstone (Fig. 8(d) and (i)–(k)). This lithofacies association is characterized by a serrated shape in the gamma ray log (Fig. 9(b)).

Interpretation. Overbanks are defined as thin-layered deposits developed along the channel flanks, formed by the overflow of turbidity currents from the channel (Kane et al., 2007; Posamentier and Walker, 2006). The cross-bedded very fine sandstone and parallel-bedded very fine sandstone correspond to the Tc and Td divisions of the Bouma sequence, respectively, which indicates a process of slow deposition as turbidity current energy decrease (Beaubouef, 2004; Kane et al., 2007).

(3) Lobe

Description. The lithofacies association within the lobe main body predominantly exhibits coarsening-upward successions or homogeneous successions (Fig. 9(c)). From its base to the top, it is characterized by thick-bedded (averaging about 30 ft, up to 100 ft) massive fine sandstone and reverse grading fine sandstone (Fig. 8(d) and (f)). Mudstone occurs rarely within this interval, and erosional surfaces are typically absent at the base. The density log response displays a funnel or cylindrical shape (Fig. 9(c)). However, toward the lobe margins, the lithofacies association transitions to finer-grained, thinner-bedded deposits with significantly increased mudstone frequency. This association consists of moderately thick interbeds (generally less than 10 ft) of massive fine or very fine sandstone, parallel-bedded very fine sandstone, and cross-bedded very fine sandstone (locally containing dish structures) (Fig. 8(e)), alternating with horizontal-bedded mudstone. While the gamma ray log also exhibits alternating cylindrical and serrated shapes (Fig. 9(d)). Furthermore, in the channel–lobe transition zone (CLTZ), a distinct architectural element known as the channelised lobe is developed. It is characterized by a composite stacking pattern, where typical lobe deposits (massive or reverse-graded sandstones) are overlain by channelized deposits (erosive-based, fining-upward sequences) (Zakaria et al., 2013).

Interpretation. Compared to channel deposits, lobes exhibit finer grain size and lack basal erosional feature, indicating a rapid decrease in turbidity current energy, enabling only finer-grained transportation (Deptuck et al., 2008; Mutti and Normark, 1987). However, the presence of reverse grading fine sandstone is a common feature associated with the transformation of high-density turbidity currents upon entering unconfined topography. It likely records rapid deposition from the flow head or a dense basal layer during initial flow expansion and deceleration (Lowe, 1982; Postma et al., 2014). The lobe facies association characterized by lack of basal erosional features and dominance of the Tb division of the Bouma sequence formed through steady deposition represents deposition from accelerated subcritical flows following hydraulic jumps of supercritical turbidity currents (Postma et al., 2014). At the lobe margins, the well-developed laminated sandstones, corresponding to the Tc division of the Bouma sequence, and their internal dish structures evidence rapid sediment accumulation following abrupt energy dissipation of turbidity currents (Allen, 1981; Lowe and LoPiccolo, 1974). The development of

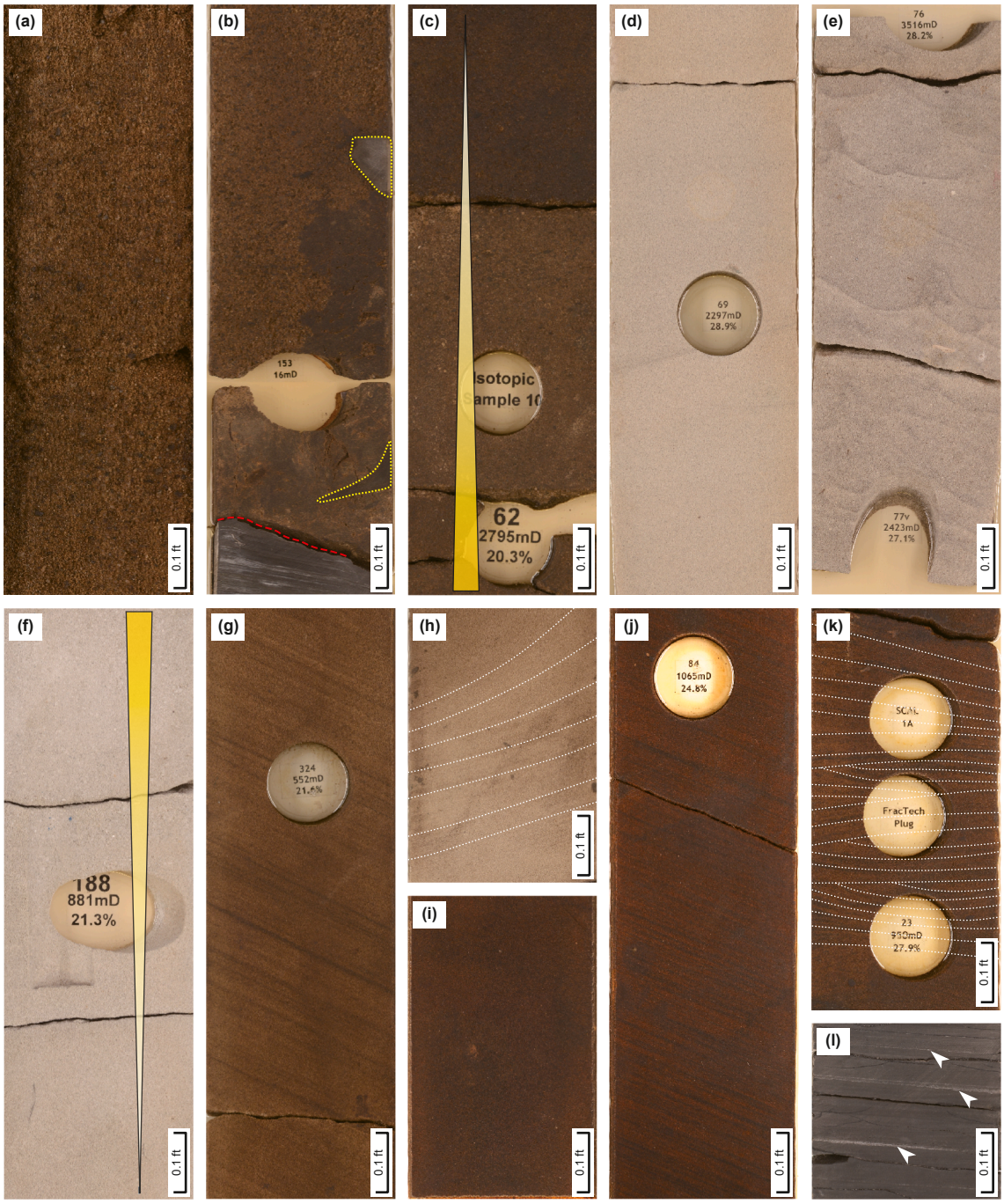

Fig. 8. Core photographs displaying the lithofacies described in the text. (**a**) Oil-bearing massive very coarse sandstone. Well P9 at 134.7 ft. (**b**) Oil-bearing massive coarse sandstone with mud clasts (yellow dotted circle) and erosional surface (red dotted line). Well P1A at 222.4 ft. (**c**) Oil-bearing normal grading medium-coarse sandstone. Well D5 at 62.5 ft. (**d**) Massive fine sandstone. Well W1 at 261.3 ft. (**e**) Massive fine sandstone with dish structure. Well W1 at 268.9 ft. (**f**) Reverse grading fine sandstone. Well D5 at 194.9 ft. (**g**) Oil-bearing parallel-bedded fine sandstone. Well P8 at 363.7 ft. (**h**) Oil-bearing cross-bedded fine sandstone. Well W1 at 290.2 ft. (**i**) Oil-bearing massive very fine sandstone. Well P1A at 167.4 ft. (**j**) Oil-bearing parallel-bedded very fine sandstone. Well P1A at 152.9 ft. (**k**) Oil-bearing cross-bedded very fine sandstone. Well P1A at 91.1 ft. (**l**) Horizontal-bedded mudstone with intercalated thin layers of siltstone (white arrows). Well Z2 at 197.6 ft.

channelised lobes within the CLTZ records a key genetic transition marked by later turbidity currents concentrating and incising channels into pre-existing lobe deposits, guided by their subtle topography (Lin et al., 2014; Prélat et al., 2009).

4.2.2. Areal distribution characteristics of individual channel–lobe

Based on the interpretation of well architectural element types (Fig. 9) and combined with the areal distribution of sand bodies within each single zone (Fig. 10), this study identifies that the channel–lobe complexes within different sand groups in the study area are composed of one or multiple individual channel–lobes (Fig. 11). These individual channel–lobes exhibit both similarities and certain differences in their areal distribution characteristics.

The similarities in areal distribution are manifested as depositional bypass in the up-dip direction for almost all individual channel–lobes (Fig. 11). In these up-dip bypass areas, which

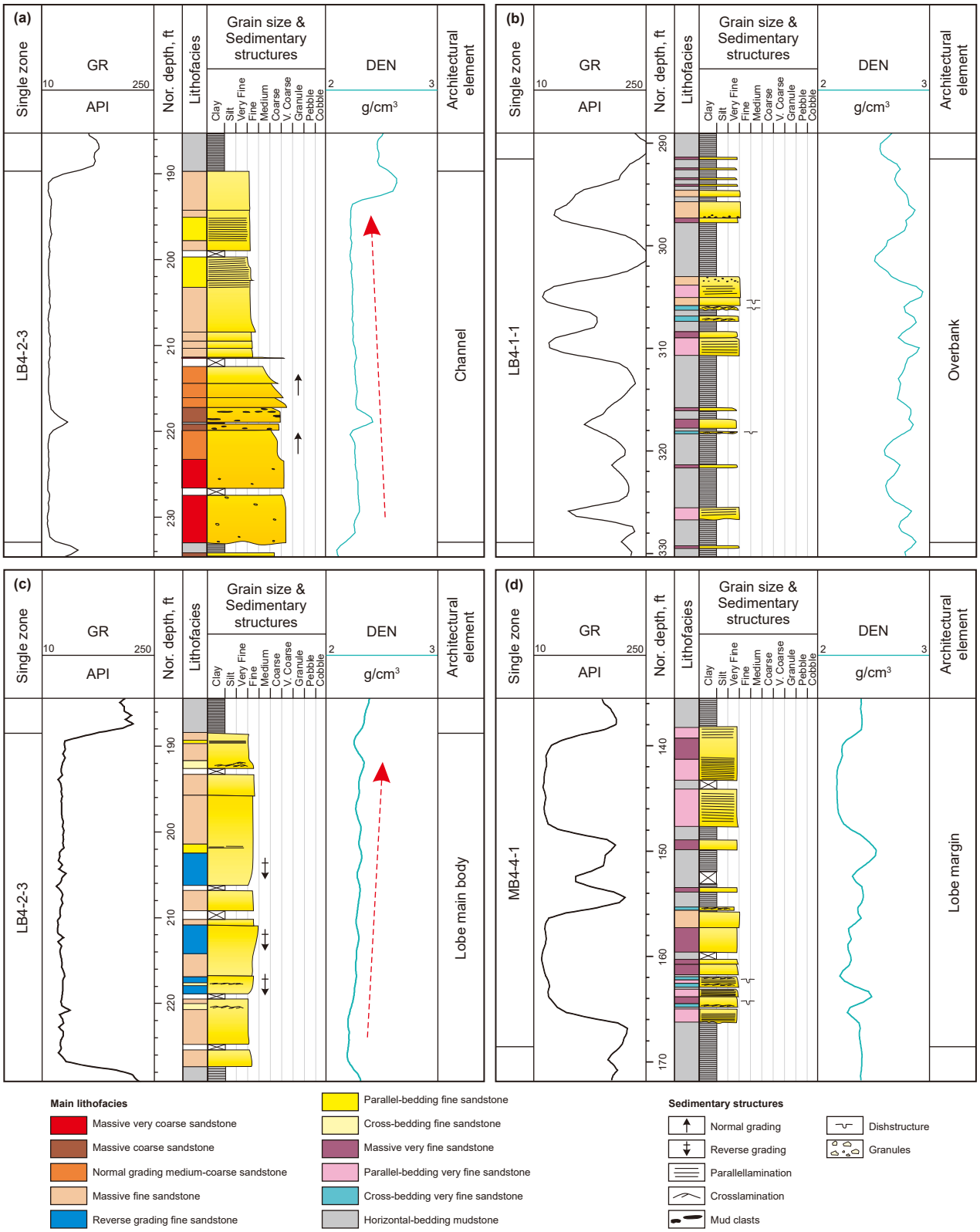

Fig. 9. Core and log response characteristics of different architectural elements in the submarine fan of the study area (well locations are shown in Fig. 11): (**a**) channel in Well P1A; (**b**) overbank in Well P1A; (**c**) lobe main body in Well A4; (**d**) lobe margin in Well P1A. Nor. Depth = normalized depth.

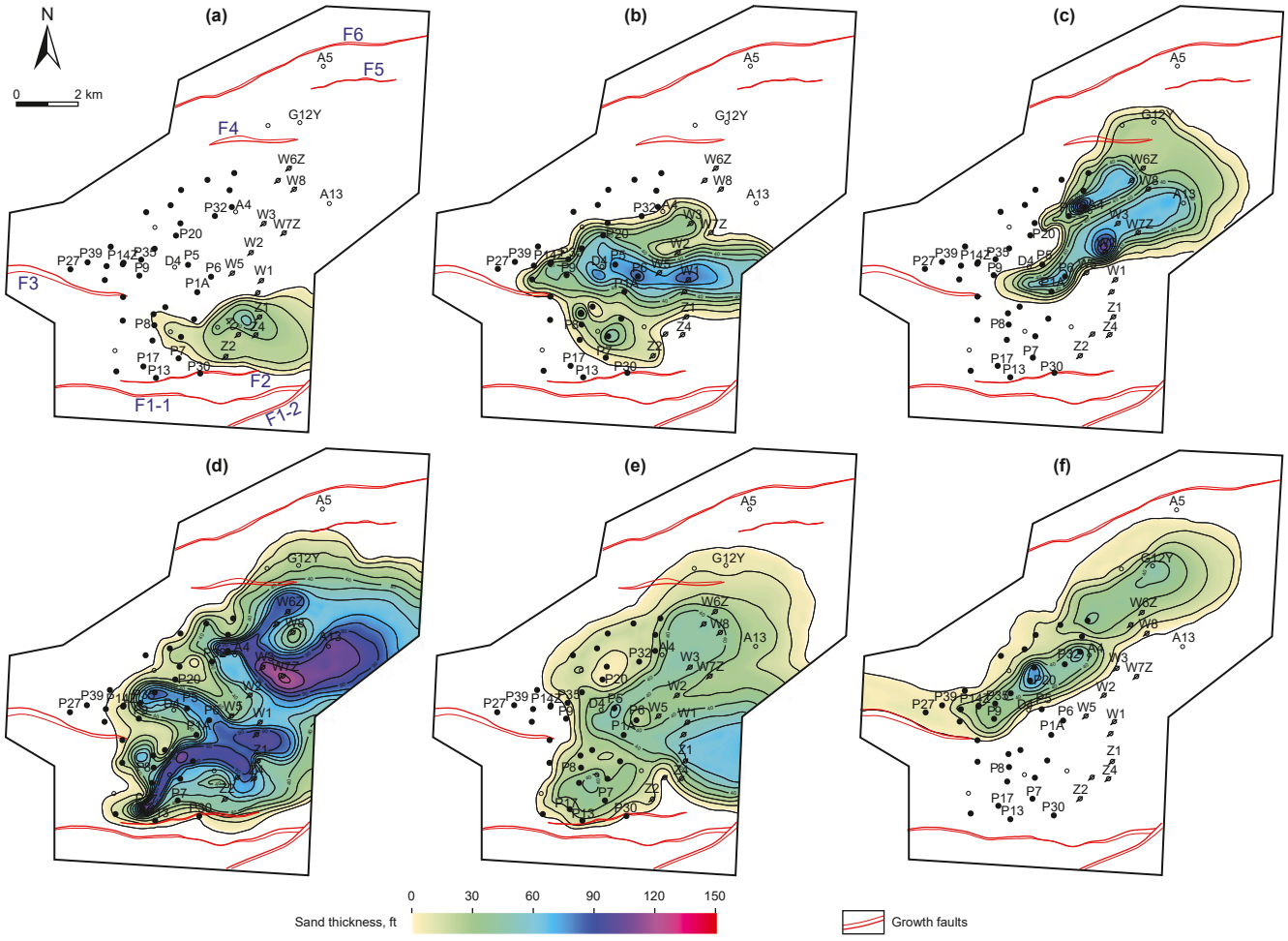

Fig. 10. Sand thickness distribution maps of typical single zones in the study area: (**a**) single zone LB4-1-2; (**b**) single zone LB4-2-2; (**c**) single zone LB4-2-3; (**d**) single zone MB4-4-2; (**e**) single zoneMB4-5-2; (**f**) single zone UB4-6-1.

consistently correspond to thin or zero sand thickness in Fig. 10, the well logs show distinctive signatures characterized by serrated, low-amplitude log facies with thin, finger-like sand bodies embedded within a mud-dominated background (Stevenson et al., 2015; Sullivan et al., 2000). A representative example can be found in well P27 at single zone MB4-4-2 (Fig. 12(b)). The presence of these bypass facies is consistently supported by the development of well-defined channels immediately downdip. Along with same evolutionary features of architectural elements along the source direction. In the proximal area, submarine fans comprise low-sinuosity belt-shaped channels flanked by overbanks. The channels exhibit a flat top and convex bottom morphology, potentially incising into underlying strata, while overbanks develop laterally adjacent to the channel margins, which is a common characteristic described in analogous fan systems (Chapin, 2007; McHargue et al., 2021; Sullivan et al., 2000). In mid-distal area, channels may bifurcate to form distributary channels and develop channelized lobes (Fig. 11(b)–(d), (e)), where channelized lobes result from successive channel stories incising and overlapping onto preexisting lobe stories (Zhang et al., 2016). In distal area, the ends of channelized lobes develop fan-shaped or tongue-shaped lobe deposits (Fig. 11), showing a flat base and convex top morphology in cross-section.

The differences in areal distribution of individual channel–lobes among different sand groups are reflected in the following aspects. Firstly, although almost all individual channel–lobes exhibit depositional bypass in the up-dip direction, the initiation point of bypass progressively migrates towards the structural highs in the western study area from lower to upper single zones (Figs. 10 and 11), which is evidenced by the concomitant westward migration of the zero-thickness line in the sand thickness maps (Fig. 10). Secondly, within the LB4 sand group, channel–lobe complexes have relatively small scale and primarily comprise 1–3 individual channel–lobes (Fig. 11(a)–(c)). This is reflected in the sand thickness maps as isolated, limited-range thick zones (Fig. 10(a)–(c)). From early to late depositional stages, their distribution shifts gradually from the southeastern to northeastern study area, and the orientation of the internal individual channel–lobes changes from nearly W–E (Fig. 11(a) and (b)) to SW–NE (Fig. 11(c)) trends. In contrast, the MB4 sand group features significantly larger-scale channel–lobe complexes composed of 4–5 individual channel-lobes (Fig. 11(d) and (e)). Correspondingly, the sand thickness maps show extensive, high-amplitude thick zones with greater lateral connectivity (Fig. 10(d) and (e)). Unlike LB4, their distribution shows no obvious migration from early to late stages, with internal individual channel–lobes extending predominantly in nearly W–E trending or SW–NE trending. Within the UB4 sand group, the complexes are consistently composed of only 2 individual channel–lobes and exhibit a reduced areal extent. Their distribution is confined to the relatively structurally high northwestern part of the study area (Fig. 10(f)), contrasting with the eastern distribution observed in lower sand groups, and the

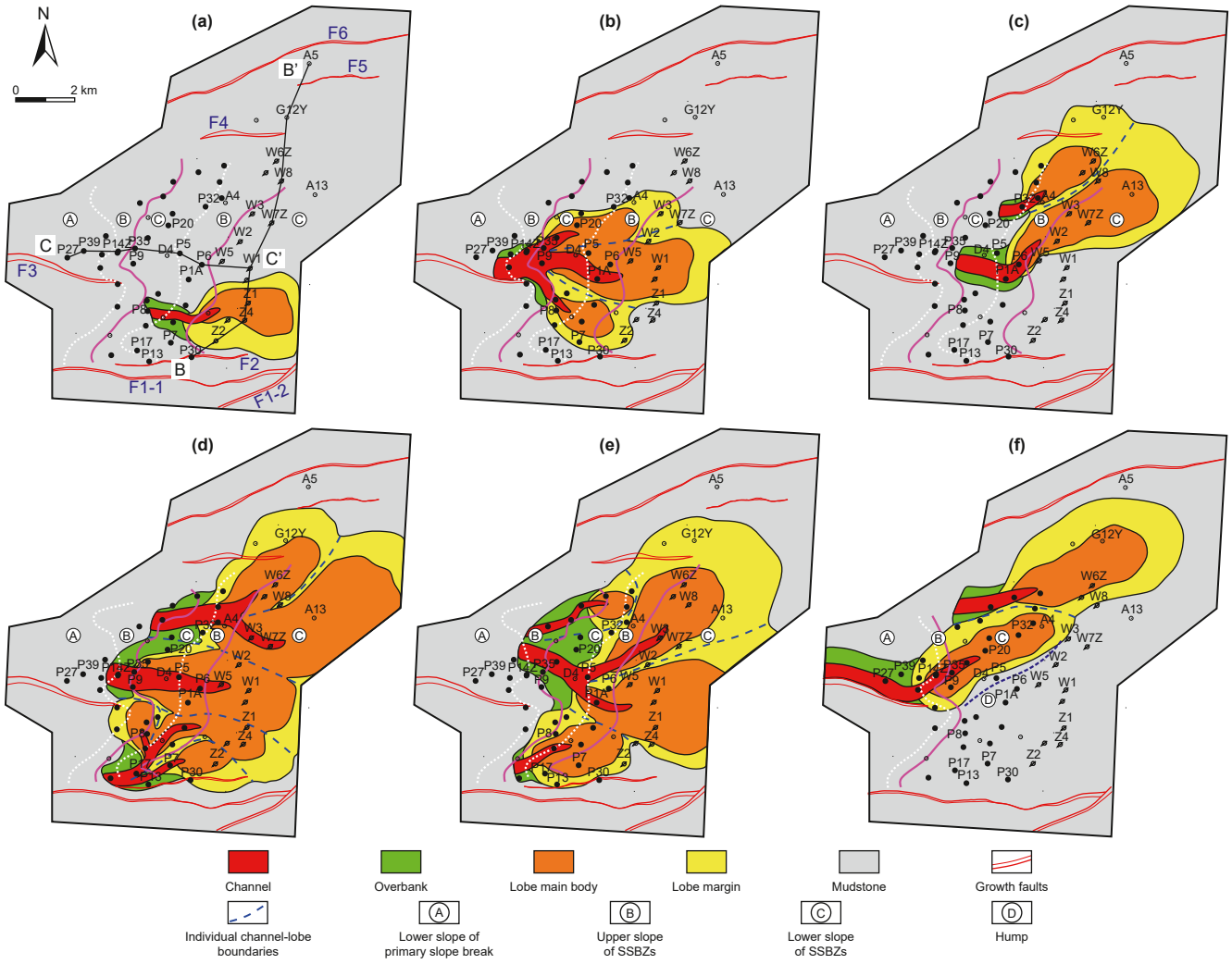

Fig. 11. Areal distribution of individual channel–lobes within typical single zones in the study area: (**a**) single zone LB4-1-2; (**b**) single zone LB4-2-2; (**c**) single zone LB4-2-3; (**d**) single zone MB4-4-2; (**e**) single zone MB4-5-2; (**f**) single zone UB4-6-1. The purple line denotes the location of the SSBZs, and the white dashed line indicates the boundary between the upper and lower slopes.

orientations of the individual channel–lobes are uniformly nearly SW–NE trends (Fig. 11(f)).

4.2.3. Vertical stacking characteristics of individual channel–lobes

Vertically, individual channel–lobes exhibit distinct stacking patterns that vary period to period, reflecting different intra-graben conditions. These patterns can be interpreted within established models of deep-water deposition (e.g., Chapin et al., 1994; Prélat et al., 2009; Zhang et al., 2016). Within the LB4 sand group, individual channel–lobes display significant lateral migration and stacking, progressively shifting northward from the southern part of the study area with high migration intensity with relatively limited overlap between individual channel–lobes (Fig. 12(a)). In contrast, the MB4 sand group exhibits relatively weaker lateral migration of individual channel–lobes from bottom to top, with these elements primarily showing compensational stacking (Fig. 12(a)). Within the UB4 sand group, lateral migration is further reduced, characterized dominantly by vertical aggradational stacking. Notably, however, the entire UB4 sand group displays a progradational stacking pattern retrograding in the source direction compared to the MB4 sand group (Fig. 12(b)), which confines the distribution of individual channel–lobes within the northwestern part of the study area (Fig. 11(f)).

4.2.4. Scale characteristics of individual channels (and lobes) within individual channel–lobes

Based on the quantitative measurements of individual channels and lobes, statistical analysis reveals the following scale characteristics and relationships.

In the study area, bifurcation angles between distributary channels range from 23° to 46°, with an average of approximately 36° (Fig. 13(a)). The average width of individual channels ranges from 0.4 to 0.6 km, the average thickness ranges from 5 to 30 m, and the average width to thickness ratio is approximately 54 (Fig. 13(a)). Individual lobes in the study area exhibit two morphologies: fan-shaped and tongue-shaped. For fan-shaped individual lobes, the maximum length ranges from 1.2 to 4.3 km, the maximum width ranges from 0.8 to 3.2 km, the average thickness is approximately 52 ft, and there is a relatively high correlation coefficient between the maximum length and maximum width (Fig. 13(b)), with an average length to width ratio of approximately 1.4. However, tongue-shaped individual lobes have a maximum length of 4.1–6.9 km, a maximum width of 1–3.1 km, an average thickness of approximately 50 ft, and a relatively poor correlation between the maximum length and maximum width (Fig. 13(b)), with an average length to width ratio of approximately 3.2.

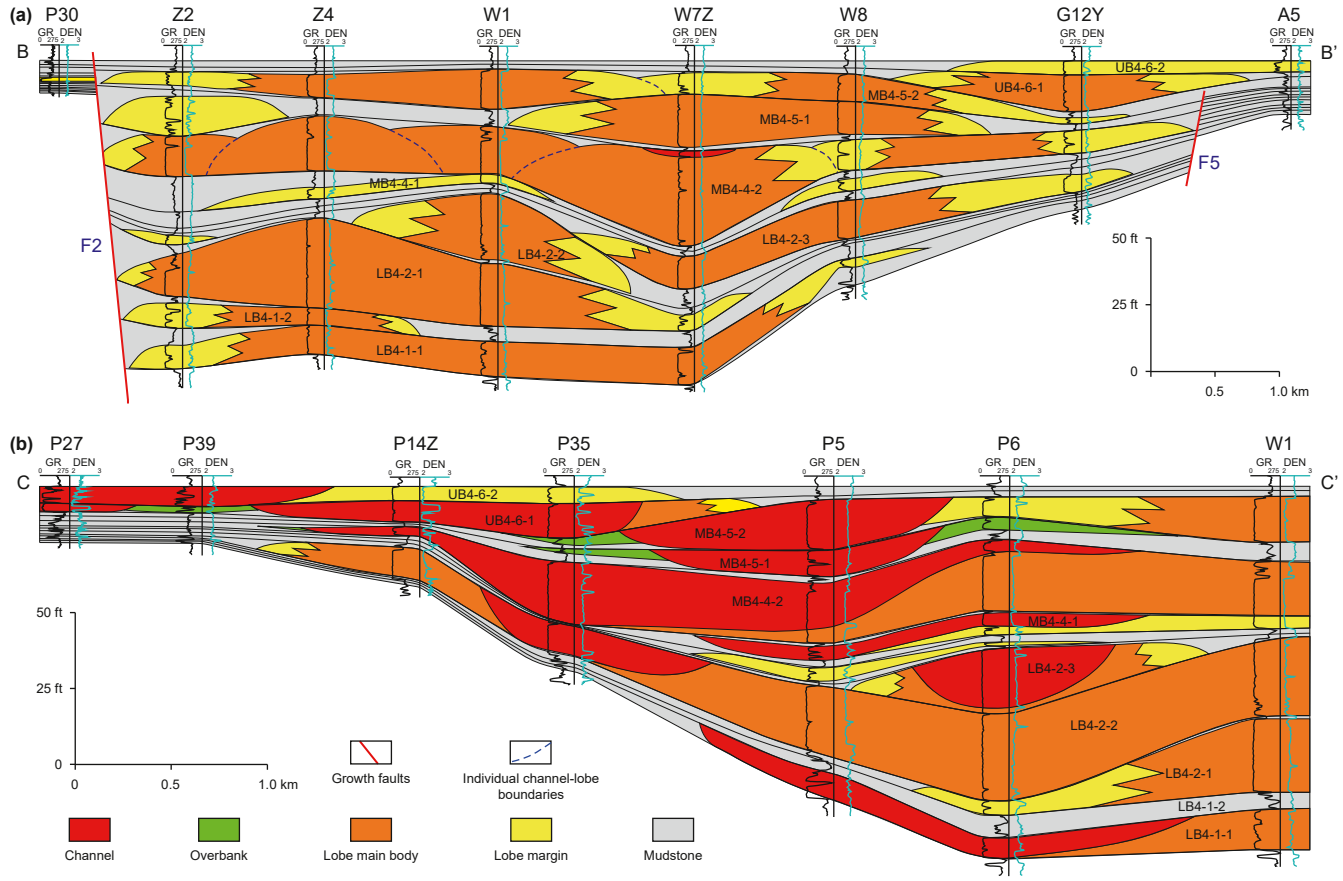

Fig. 12. Cross-well profiles of individual channel–lobe architecture features along (**a**) and across (**b**) source directions in the study area. Profile locations are shown in Fig. 11(a).

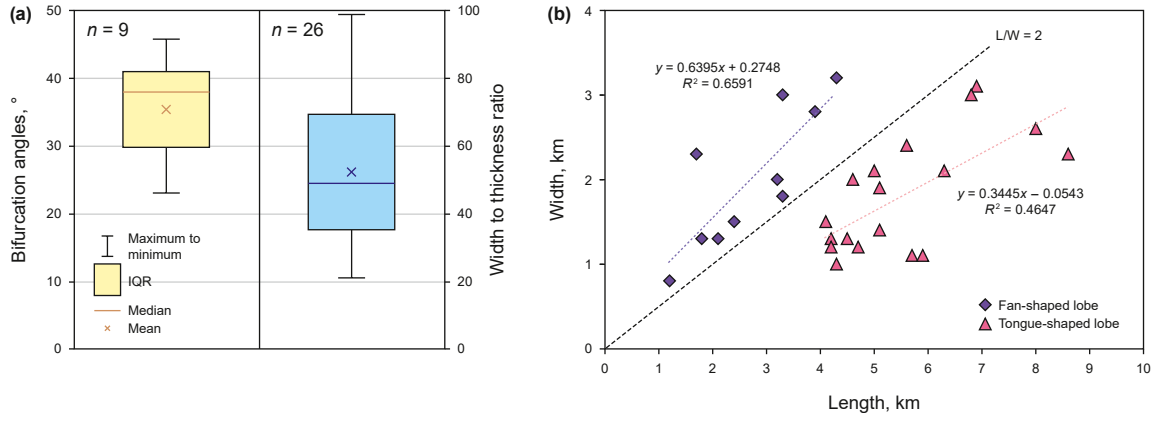

Fig. 13. (**a**) Left box plot showing bifurcation angles between distributary channels and right box plot showing width to thickness ratios of individual channels, (**b**) scatter plot of average length versus average width for individual lobes, where tongue-shaped lobes have length to width ratios more than 2 and fan-shaped lobes less than 2.

5. Discussion

5.1. Control of paleo-geomorphology on depositional architecture of axial submarine fans

The formation and evolution of the submarine fan depositional architecture are influenced by a combination of multiple factors, consequently exhibiting complex distribution characteristics. Although numerous previous research have demonstrated that the depositional architectural features of submarine fans are affected by extra-basinal factors such as source type, sea-level, climate change, and bottom currents (Chen et al., 2024b; Fonnesu et al., 2020; Gong et al., 2016, 2018; Normark et al., 1998; Richards et al., 1998; Stow et al., 1984; Zhang et al., 2018), the intra-basin (or intra-graben) geomorphological feature remain the most direct controlling factor (Bell et al., 2018; Chen et al., 2024a; Leeder and Gawthorpe, 1987; Moody et al., 2012; Picot et al., 2016; Zhang et al., 2016). Geomorphological features (such as topographic slope, tectonic relief, basin basement morphology, etc.) paly a decisive role in the architectural characteristics of the submarine

fan channel–lobe systems by influencing sediment gravity flow supply pathways, hydrodynamic mechanisms, and sediment distribution patterns.

As previously discussed, the axial submarine fan within the B4 oil group is characterized by sand-rich, lobe-dominated deposits with low-sinuosity channels. This sedimentary character suggests high sediment supply efficiency, which can be linked to a background of relatively arid climate and relatively low sea level during this period (Hesselbo, 2008; Hesselbo et al., 2009). While these regional factors preconditioned the system to be sediment-rich, the detailed internal architecture, including its areal distribution and stacking patterns, was primarily governed by the local paleo-geomorphology. We therefore focus the subsequent discussion on the critical control that the paleo-geomorphic configuration (featuring axial stepped slope breaks and phased transverse confinement changes) exerted on the axial submarine fan's internal architecture. This will be discussed in the following two aspects.

5.1.1. Axial slope variations control downstream evolution of individual channel–lobes

The axial stepped slope breaks in the study area primarily resulted from pre-existing basement topography and differential activity of the graben-boundary fault F1-1, with minimal influence from differential compaction of the underlying mud-rich B0-B3 intervals. During the syn-rift setting, the developed paleo-geomorphology exhibits distinct stepped slope breaks axially, which fundamentally control the downstream transformation of high-density turbidity currents and associated architectural elements. Based on quantitative slope data, we delineate four geomorphic zones axially: extremely steep slope segment, steep slope segment, slope transition zone, and gentle slope segment.

(1) Extremely steep slope segment (greater than 7°)

West of the study area, on the upper slope of the primary slope break (approximately 7.5°) (Fig. 14), high-density turbidity currents maintain high transport velocities, dominantly bypassing sediments without deposition. Pohl et al. (2020) confirmed through flume experiments that when upper slopes exceed 6°, efficient turbidity currents favor sediment bypass, causing pinch-out points to occur on the lower slope of slope breaks. These experimental results explain why all channel elements in the study area pinch out westward (lower slope of primary slope break), essentially resulting from sediment bypass induced by the extremely steep upper slope.

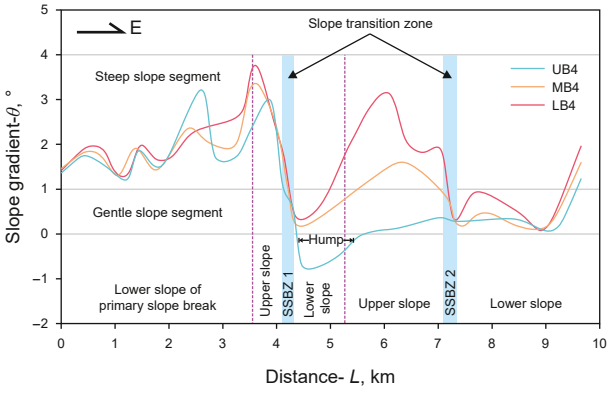

Fig. 14. Axial paleo-geomorphology slope gradient across stepped slope breaks and associated geomorphic zones during deposition of different sand groups in the study area. Positive slope gradient values indicate eastward-dipping paleo-geomorphology; negative values denote westward dip. Only the hump during UB4 sand group deposition exhibits a negative slope gradient value. Section location shown in Fig. 6.

(2) Steep slope segment (between 1° and 4°)

In steep slope segment (e.g., upper slope of SSBZ1 in MB4 sand group, with a slope gradient of approximately 3.3°) (Fig. 14), high-density turbidity currents sustain high-speed and high-energy transport, locally eroding underlying strata. This causes localized thinning of interbedded mudstones (e.g., at the UB4-4-2 single zone in Well P35 of Fig. 12(b)) and develops relatively homogeneous massive very coarse sandstones above erosional surfaces (Fig. 9(a)). Following supercritical flow identification characteristics (Postma and Cartigny, 2014; Postma et al., 2014), we suggest these erosion-fill features as evidence of supercritical turbidity currents on steep slope segment. Under steep slope, supercritical flows maintain high velocities primarily through gravitational acceleration, with subdued turbulent effects limiting lateral diffusion. This promotes vertical incision, forming relatively straight single channels flanked by overbank deposits. Notably, the upper slope of SSBZ2 evolved from steep (2.8° in LB4) to filled and vanished in UB4, reducing its ability to accelerate turbidity currents and generate erosion. This explains diminished channel development in MB4 and UB4 sand groups.

(3) Slope transition zone (slope gradient decline rate $\Delta\theta/\Delta L$ greater than 2°/km)

In slope transition zones (e.g., near SSBZ1 of the MB4 sand group, where the slope gradient rapidly decreases from approximately 3.3° to approximately 0.1° over a distance of 0.4 km, with slope gradient decline rate $\Delta\theta/\Delta L$ of 7.95°/km) (Fig. 14), abrupt slope gradient reduction diminishes gravitational components while enhancing bed friction and internal flow resistance. Rapid energy dissipation through hydraulic jumps triggers the transition of turbidity currents from supercritical to subcritical flow (Cartigny et al., 2014; Postma and Cartigny, 2014). Core photographs downstream of SSBZ1 in the MB4 sand group show widely distributed fine sandstones with rich bedded structures (Figs. 8(g) and (h) and 9(c)) confirming this transformation. More importantly, the rapid decrease in turbidity current velocity significantly enhances lateral diffusion, producing divergent flow patterns (Kneller, 1995). This drives channel bifurcation into 2–3 distributary channels that gradually splay to form channelized lobes, or develop crevasse splays and overbank deposits between distributary channels.

(4) Gentle slope segment (less than 1°)

In the gentle slope segment (e.g., the lower slope of SSBZ2 in the LB4 sand group, with a slope gradient of approximately 0.5°) (Fig. 14), energy depletion in subcritical turbidity currents gradually reduces sediment concentration, transforming flows into low-energy turbidity currents (Shanmugam et al., 1994). Enhanced fluid diffusion promotes large scale sediment deposition, forming thick individual lobes.

Quantitative analysis demonstrates that the axially developed stepped slope breaks exert significant control on the quantitative scale characteristics of submarine fan architectural elements. Statistical analysis of bifurcation angles of individual distributary channels and the corresponding slope gradient decline rates ($\Delta\theta/\Delta L$) within slope transition zones during their deposition reveals a distinct correlation between channel bifurcation development/bifurcation angles and the slope gradient decline rates (Fig. 15(a)). A slope gradient decline rates ($\Delta\theta/\Delta L$) exceeding 2°/km

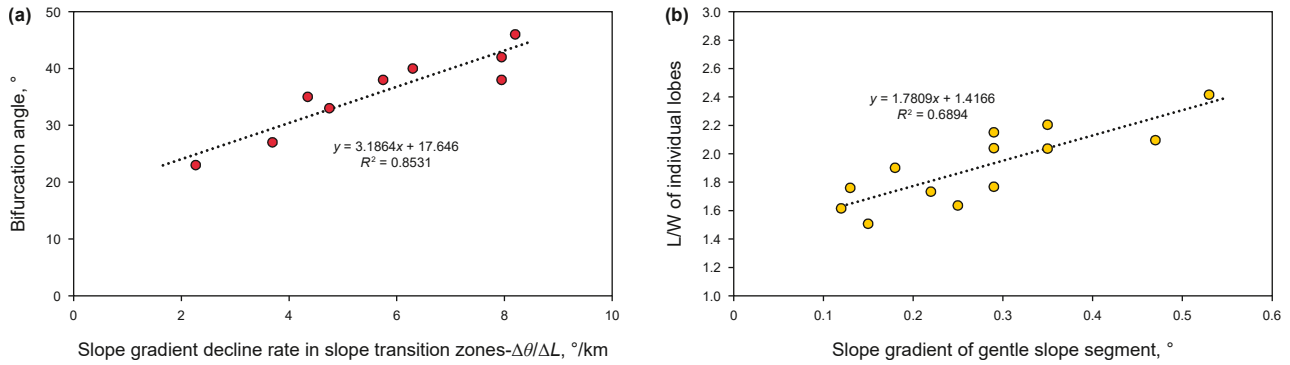

Fig. 15. (**a**) Scatter plot of correlation analysis between bifurcation angles of individual distributary channels and slope gradient decline rates ($\Delta\theta/\Delta L$) within slope transition zones, (**b**) scatter plot of correlation analysis between slope gradients of gentle slope segments and length to width ratios (L/W) of individual lobes.

represents the critical threshold for bifurcation in individual channels. When $\Delta\theta/\Delta L$ exceeds 2°/km, the bifurcation angle increases positively with the slope gradient decline rate within the slope transition zone, reflecting that faster gradient reduction promotes greater divergence of turbidity currents. Furthermore, the gradient of gentle slope segments exhibits a significant positive correlation with the length to width ratio of deposited lobes (Fig. 15(b)). Lower gradients on gentle slopes facilitate rapid sediment accumulation, favoring the formation of fan-shaped individual lobes, whereas higher gradients promote tongue-shaped individual lobes.

5.1.2. Transverse confinement controls stacking types of individual channel–lobes

The graben boundary faults (F1-1, F1-2, and F6) broadly constrain the distribution of the submarine fan. During deposition of different sand groups, lateral confinement within the graben evolved through three stages, resulting in distinct stacking patterns of individual channel–lobes among sand groups.

(1) Transversely asymmetric geomorphic stage (deposition of the LB4 sand group)

Under asymmetric slopes caused by differential throws of graben boundary faults, the paleo-geomorphology exhibited transverse asymmetry in confinement. Transversely, the southern graben features a steep slope (slope gradient approximately 4.3°) with high confinement, while the northern graben has a gentle slope (slope gradient approximately 0.7°) with low confinement. A narrow trough (width about 4 km) developed on the lower slope of SSBZ2 (Fig. 7(b)). Driven by gravitational potential energy, high-density turbidity currents were consistently transported to this narrow trough at the topographic low (Fig. 11(a)). Individual channel–lobes preferentially deposited near the steep slope where confinement was stronger (Zhang et al., 2016). As deposition proceeded, subsequent individual channel–lobes progressively migrated toward the gentler, less confined side, resulting in a lateral migration stacking pattern (Fig. 12(a)).

(2) Transversely symmetric geomorphic stage (deposition of the MB4 sand group)

Sediment filling during the LB4 stage flattened the troughs and thus formed a transversely symmetric, gentle paleo-geomorphology with significantly reduced confinement. (Fig. 7(b)). Under this setting, turbidity currents readily dispersed, expanding sediment unloading areas and increasing the planar area of individual channel–lobes compared to the previous stage. Stacking patterns were primarily controlled by depositional processes: when channels bifurcated or avulsed, subsequent individual channel–lobes preferentially filled local topographic lows created by prior deposits, showing an unordered compensational stacking pattern (Fig. 12(a)).

(3) Locally confined geomorphic stage (deposition of the UB4 sand group)

Continued infilling during the MB4 stage caused local topographic inversion, forming a banded hump that combined with growth fault F3 to create a new transverse barrier (Figs. 6 and 7(a)). This forced channels to deflect by 60°–80°, depositing individual channel–lobes in topographic lows up-dip of the hump (Fig. 11(f)). Consequently, individual channel–lobes within the UB4 sand group exhibit a retrogradational stacking pattern relative to the MB4 stage (Fig. 12(b)).

5.1.3. Dynamic feedback between depositional architecture and paleo-geomorphology

The “axial stepped slope breaks–transverse confinement” paleo-geomorphology characterized above represents a foundational control framework. However, the evolution of the axial submarine fan depositional architecture was not a passive filling of a static template but involved dynamic feedback loops, whereby the deposits themselves began to influence the paleo-geomorphology and subsequent flows.

This study identifies key evidence of these interactions: in the MB4 sand group, the extensive compensational stacking of lobes indicates that the transversely symmetric topography created by earlier deposits actively guided later turbidity currents. After channel bifurcation in the slope transition zone, this depositionally constructed topography facilitated the lateral spreading and broader distribution of flows, leading to the development of widespread, sheet-like channel–lobe complexes (Figs. 10(d) and 11(d)). Concurrently, growth fault activity (e.g., Fault F3) provided an external driver that continuously regenerated accommodation space and slope gradients, sustaining sediment bypass in up-dip areas (Fig. 11).

In conclusion, the architectural pattern of the B4 axial submarine fan is the product of a complex interplay. The initial and tectonically evolving paleo-geomorphology set the fundamental constraints, but the system's detailed architecture was ultimately influenced by the dynamic feedback mechanisms, whereby the deposits themselves became one of the controls on subsequent sedimentation.

5.2. Dual-factor coupling control model of submarine fan depositional architecture: "axial stepped slope breaks–transverse confinement"

Traditional submarine fan studies have mostly been based on static geomorphic settings, emphasizing facies differentiation across slope breaks–such as the influence of the presence or absence of slope breaks on the distribution of submarine fan depositional systems (Garcia and Parker, 1989; Hodgson et al., 2022; Pohl, 2019). In recent years, scholars have gradually recognized that the dynamic changes of paleo-geomorphology controls submarine fan sedimentary processes and depositional architectures. For example, studies in the thrust belts of the West African continental slope have shown that differences in geomorphic confinement formed during different stages of thrust tectonic evolution control the spatial differential distribution of channels and lobes (Lin et al., 2018). In rift basins, previous studies have separately considered submarine fan distribution patterns controlled by the evolution of transfer zones (Jackson et al., 2011; Tillmans et al., 2021), transverse fault terraces (Henstra et al., 2017; Tillmans et al., 2021), and laterally confining geomorphology formed by growth faults (Tian et al., 2024). However, these studies mostly focus on the influence of a single factor, lacking systematic analysis of the dynamic response of submarine fan depositional architectures to the coupling of "slope-confinement" dual factors.

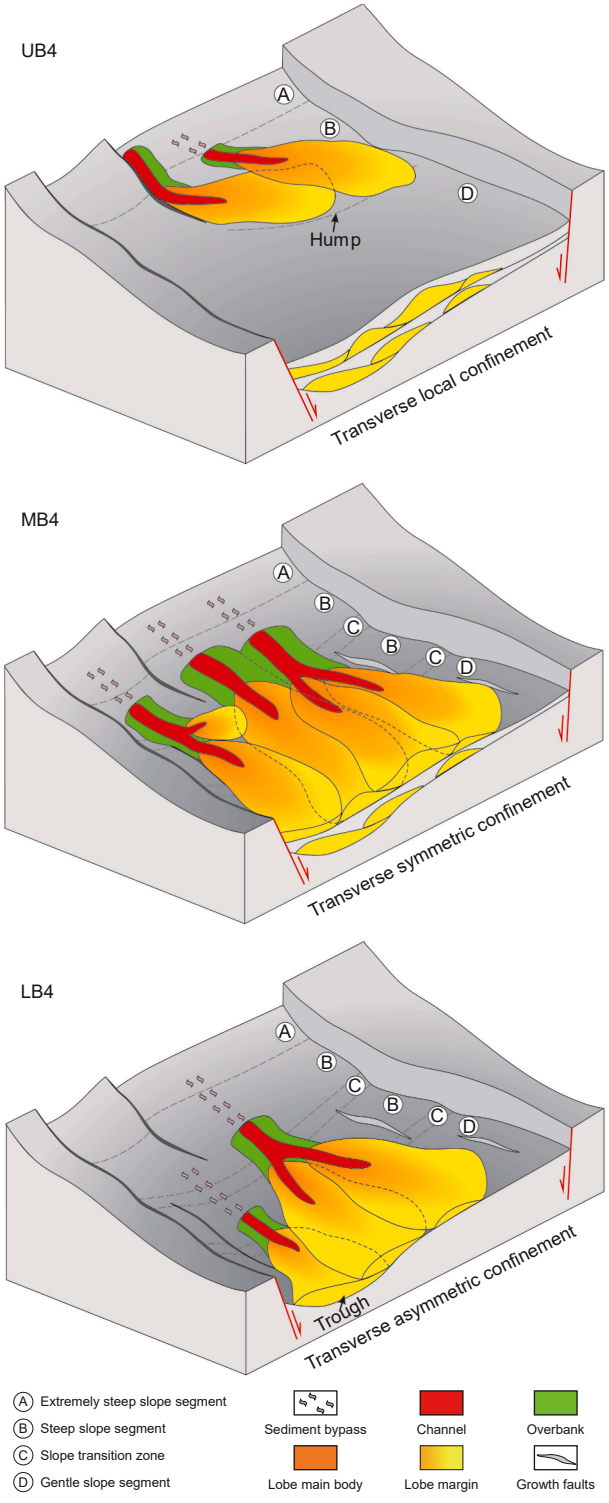

Fig. 16. Depositional architecture model of individual channel–lobe under the coupled control of axial stepped slope breaks and transverse confinement during the depositional stages of different sand groups.

Through the analysis of submarine fans in the rift basin of the North Sea, UK, this study reveals that axial stepped slope breaks and transverse confinement variations of paleo-geomorphology jointly constitute the core controls on the evolution of submarine fan architectures. As the axial slope transitions from the extremely steep slope segment, steep slope segment, and slope transition zone to the gentle slope segment, architectural elements evolve from sediment bypass to individual channels with overbanks, form distributary channels and channelized lobes in the slope transition zone, and finally accumulate into lobes in the gentle slope segment. In the slope transition zone where the slope gradient rapidly decreases from steep to gentle, the bifurcation angles between distributary channels increase with the rise in slope gradient decline rate. Meanwhile, the transition of transverse confinement from asymmetric to symmetric and then to local confinement causes the stacking patterns of individual channel–lobes to evolve from lateral migration to unordered compensation, and further to deflected retrogradation (Fig. 16).

This model therefore represents not only a static control framework but also a dynamic system, as the initial topography and its subsequent modification by deposition collectively governed the architectural evolution.

6. Conclusion

(1) This study reveals the "axial stepped slope breaks–transverse confinement" paleo-geomorphic characteristics and their controls on the depositional architecture of individual channel-lobe systems within axial submarine fans of the Upper Jurassic B4 oil group in the North Sea X Oilfield. The submarine fan exhibits distinct axial and vertical spatial distribution patterns. Along axial stepped slope breaks, architectural elements evolve from sediment bypass to channel–overbank systems, then to distributary channels and channelized lobes, and finally accumulate into lobes. Vertically, three patterns are identified: in the early stage (LB4), limited-scale tongue-shaped lobes develop predominantly in the east, showing lateral migration stacking northward; in the middle stage (MB4), multiple individual channel–lobes develop extensively, forming large-scale, regionally continuous fan-shaped lobes that exhibit unordered compensational stacking; in the late stage (UB4), the distribution range of individual channel–lobes contracts, causing the depositional center to shift northwestward and

exhibit a retrogradational stacking pattern relative to the previous stage.

(2) Axial stepped slope breaks govern downstream evolution of architectural elements by triggering turbidity current transformations. On extremely steep slope (gradient about 7.5°), supercritical flows dominate erosion and bypass; on steep slopes (gradient between 1° and 4°), supercritical flows cause significant erosion, forming incised channels. In slope transition zones with rapid gradient decline ($\Delta\theta/\Delta L$ greater than 2°/km), hydraulic jumps induced energy dissipation and flow divergence, promote channel bifurcation with angles positively correlated to gradient decline, and lead to the development of distributary channels and channelized lobes. On gentle slopes (gradient less than 1°), low-energy flows diffuse to form lobes, with length to width ratios positively correlated to gradient.

(3) The phased changes in transverse geomorphic confinement (from asymmetric to symmetric, then to local confinement) control the evolution of individual channel–lobe stacking patterns through redistributing accommodation. In the asymmetric stage (LB4), asymmetric graben (southern slope 4.3° vs. northern slope 0.7°) forces deposition near the steep slope with stronger confinement, causing subsequent individual channel–lobes to migrate toward the gentler side, and form lateral migration stacking. In the symmetric stage (MB4), reduced asymmetry and flattened topography lead to unordered compensational stacking as individual channel–lobes fill local topographic lows created by prior deposits. In the locally confined stage (UB4), a banded hump combined with growth fault F3 deflects channels by 60°–80° and deposits individual channel–lobes in topographic lows up-dip of the hump, resulting in a retrogradational stacking pattern.

(4) The evolution of the fan architecture was governed by a dynamic feedback mechanism. While the antecedent paleo-geomorphology set the initial template, the depositional system itself became an active agent, as the topography constructed by earlier deposits (e.g., lobe complexes) subsequently influenced the pathways and distribution of later turbidity currents.

Our study proposes a geomorphic control model for submarine fan architectures, emphasizing that paleo-geomorphic changes directly control element distribution by altering flow paths and energy, while the depositional architecture itself provides feedback that modifies subsequent sedimentation. This model provides a new perspective for deep-water depositional models, and future work should further combine flume experiments to quantify the relationships between slope (or transverse confinement), fluid dynamics, and depositional response, to establish a more comprehensive model.

CRediT authorship contribution statement

Ji-Tao Yu: Writing – review & editing, Writing – original draft, Visualization, Validation, Supervision, Software, Resources, Project administration, Methodology, Investigation, Formal analysis, Data curation, Conceptualization. **Sheng-He Wu:** Writing – review & editing, Project administration, Methodology, Funding acquisition, Formal analysis, Conceptualization. **Ming-Ming Qi:** Validation, Supervision, Resources, Investigation. **Zhen-Hua Xu:** Visualization, Validation, Supervision, Methodology. **Shu-Chun Cao:** Supervision, Project administration, Formal analysis. **Wei Du:** Software, Methodology, Data curation. **Jing-Jing Li:** Software, Methodology, Data curation. **Yu-Fei Zhang:** Software, Data curation. **Han Liu:** Visualization, Software. **Muhammad Ubaid Umar:** Software.

Declaration of competing interest

The authors declare that they have no known competing financial interests or personal relationships that could have appeared to influence the work reported in this paper.

Acknowledgements

This study is supported by Science Foundation of China University of Petroleum, Beijing (No. 2462025BJRC005) and Major Science and Technology Projects of China National Offshore Oil Corporation (CNOOC) (CBJ-2023-PCPS-0008-RI).

References

Allen, J., 1981. An occurrence of dish structures in Caradoc turbidites, Poppit Sands, near Cardigan, Dyfed, Wales. PGA 92, 75–77. https://doi.org/10.1016/S0016-7878(81)80021-1.

Allen, J., 1982. Sedimentary structures: Their character and physical basis. Elsevier, Amsterdam, p. 593.

Beaubouef, R.T., 2004. Deep-water leveed-channel complexes of the Cerro Torro Formation, Upper Cretaceous, southern Chile. AAPG Bull. 88 (11), 1471–1500. https://doi.org/10.1306/06210403130.

Bell, D., Stevenson, C.J., Kane, I.A., Hodgson, D.M., Poyatos-Moré, M., 2018. Topographic controls on the development of contemporaneous but contrasting basin-floor depositional architectures. J. Sediment. Res. 88, 1166–1189. https://doi.org/10.2110/jsr.2018.58.

Bouma, A.H., 1962. Sedimentology of some flysh deposits: A graphic approach to facies interpretation. Elsevier, Amsterdam, p. 168.

Cartigny, M.J.B., Ventra, D., Postma, G., van Den Berg, J.H., 2014. Morphodynamics and sedimentary structures of bedforms under supercritical-flow conditions: New insights from flume experiments. Sedimentology 61, 712–748. https://doi.org/10.1111/sed.12076.

Chapin, M.A., Davies, P., Gibson, J.L., Pettingill, H.S., 1994. Reservoir architecture of turbidite sheet sandstones in laterally extensive outcrops, Ross Formation, western Ireland. In: Weimer, P., Bouma, A.H., Perkins, B.F. (Eds.), Gulf Coast Section Society of Economic Paleontologists and Mineralogists Foundation Fifteenth Annual Research Conference: Submarine Fans and Turbidite Reservoirs, pp. 53–68.

Chapin, M., 2007. Amalgamated sheet and channel sandstones at Kilbaha Bay, Ross Formation, Ireland. In: Nilsen, T.H., Shew, R.D., Steffens, G.S., Studlick, J.R.J. (Eds.), Atlas of deep-water Outcrops. AAPG Studies in Geology, pp. 201–206.

Chen, M., Wu, S.H., Wang, R.F., Zhang, J.J., Xie, P.F., Wang, M., Wang, X.F., Yu, J.T., Xiong, Q.C., 2024a. Sedimentary architecture of submarine channel-lobe systems under different seafloor topography: Insights from the Rovuma Basin offshore East Africa. Pet. Sci. 21, 125–142. https://doi.org/10.1016/j.petsci.2023.11.021.

Chen, M., Wu, S.H., Wang, R.F., Zhang, J.J., Xie, P.F., Wang, M., Wang, X.F., Xiong, Q.C., Yu, J.T., Miramontes, E., 2024b. Sedimentary architecture of submarine lobes affected by bottom currents: Insights from the Rovuma Basin offshore East Africa. Basin Res. 36, e12829. https://doi.org/10.1111/bre.12829.

Copestake, P., Partington, M.A., 2023. Sequence stratigraphy scheme for the uppermost middle jurassic-lowermost Cretaceous of the North Sea area. In: Copestake, P., Partington, M.A. (Eds.), Sequence Stratigraphy of the Jurassic-Lowermost Cretaceous (Hettangian-Berriasian) of the North Sea Region. Geological Society, London, pp. 135–214. https://doi.org/10.1144/M59-2022-70.

Coward, M.P., Dewey, J.F., Hempton, M., Holroyd, J., 2003. Tectonic evolution. In: Evans, D., Graham, C., Armour, A., Bathurst, P. (Eds.), The Millennium Atlas—Petroleum Geology of the Central and Northern North Sea. Geological Society of London, London, pp. 17–33. https://doi.org/10.1017/S0016756803218124.

Cowie, P., Underhill, J., Behn, M., Lin, J., Gill, C., 2005. Spatio-temporal evolution of strain accumulation derived from multi-scale observations of late Jurassic rifting in the northern North sea: A critical test of models for lithospheric extension. Earth Planet Sci. Lett. 234, 401–419. https://doi.org/10.1016/j.epsl.2005.01.039.

Deptuck, M.E., Piper, D.J.W., Savoye, B., Gervais, A., 2008. Dimensions and architecture of late Pleistocene submarine lobes off the northern margin of East Corsica. Sedimentology 55 (4), 869–898. https://doi.org/10.1111/j.1365-3091.2007.00926.x.

Dore, G., Robbins, J., 2005. The buzzard field. In: Petroleum Geology: North-West Europe and Global Perspectives—Proceedings of the 6th Petroleum Geology Conference. Geological Society, London, pp. 241–252. https://doi.org/10.1144/0060241.

Erratt, D., Thomas, G.M., Wall, G.R.T., 1999. The evolution of the Central North Sea Rift. In: Petroleum Geology of Northwest Europe: Proceedings of the 5th

Conference. Geological Society, London, pp. 63–82. https://doi.org/10.1144/0050063.
Fonnesu, M., Palermo, D., Galbiati, M., Marchesini, M., Bonamini, E., Bendias, D., 2020. A new world-class deep-water play-type, deposited by the syndepositional interaction of turbidity flows and bottom currents: The giant Eocene coral field in northern Mozambique. Mar. Petrol. Geol. 111, 179–201. https://doi.org/10.1016/j.marpetgeo.2019.07.047.
Fraser, S.I., Robinson, A.M., Johnson, H.D., Underhill, J.R., Kadolsky, D.G.A., Connell, R., Johannesson, P., Ravnås, R., 2003. Upper Jurassic. In: Evans, D., Graham, C., Armour, A., Bathurst, P. (Eds.), The Millennium Atlas— Petroleum Geology of the Central and Northern North Sea. Geological Society of London, London, pp. 157–189. https://doi.org/10.1017/S0016756803218124.
Garcia, M., Parker, G., 1989. Experiments on hydraulic jumps in turbidity currents near a canyon-fan transition. Science 245, 393–396. https://doi.org/10.1126/science.245.4916.393.
Gawthorpe, R.L., Leeder, M.R., 2000. Tectono-sedimentary evolution of active extensional basins. Basin Res. 12, 195–218. https://doi.org/10.1111/j.1365-2117.2000.00121.x.
Gawthorpe, R.L., Hurst, J, M, 1993. Transfer zones in extensional basins: Their structural style and influence on drainage development and stratigraphy. J. Geol. Soc. 150, 1137–1152. https://doi.org/10.1144/gsjgs.150.6.1137.
Ge, Z., Nemec, W., Gawthorpe, R.L., Rotevatn, A., Hansen, E.W.M., 2018. Response of unconfined turbidity current to relay-ramp topography: Insights from process-based numerical modelling. Basin Res. 30, 321–343. https://doi.org/10.1111/bre.12255.
Gong, C., Wang, Y., Rebesco, M., Salon, S., Steel, R.J., 2018. How do turbidity flows interact with contour currents in unidirectionally migrating deep-water channels? Geology 46, 551–554. https://doi.org/10.1130/G40204.1.
Gong, C., Wang, Y., Steel, R.J., Peakall, J., Zhao, X., Sun, Q., 2016. Flow processes and sedimentation in unidirectionally migrating deep-water channels: From a three-dimensional seismic perspective. Sedimentology 63, 645–661. https://doi.org/10.1111/sed.12233.
Guariguata-Rojas, G.J., Underhill, J.R., 2017. Implications of early Cenozoic uplift and fault reactivation for carbon storage in the Moray Firth basin. Interpretation 5, SS1–SS21. https://doi.org/10.1190/int-2017-0009.1.
Gupta, S., Underhill, J.R., Sharp, I.R., Gawthorpe, R.L., 1999. Role of fault interactions in controlling synrift sediment dispersal patterns; Miocene, Abu Alaqa Group, Suez Rift, Sinai, Egypt. Basin Res. 11, 167–189. https://doi.org/10.1046/j.1365-2117.1999.00300.x.
Henstra, G.A., Gawthorpe, R.L.H.W., Ravnas, R., Rotevatn, A., 2017. Depositional systems in multiphase rifts: Seismic case study from the Lofoten margin, Norway. Basin Res. 29, 447–469. https://doi.org/10.1111/bre.12183.
Hesselbo, S.P., 2008. Sequence stratigraphy and inferred relative sea-level change from the onshore British Jurassic. PGA 119, 19–34. https://doi.org/10.1016/S0016-7878(59)80069-9.
Hesselbo, S.P., Deconinck, J., Huggett, J.M., Morgans-Bell, H.S., 2009. Late Jurassic palaeoclimatic change from clay mineralogy and gamma-ray spectrometry of the Kimmeridge Clay, Dorset, UK. J. Geol. Soc. 166, 1123–1133. https://doi.org/10.1144/0016-76492009-070.
Higley, D., 2004. The Talara Basin province of Northwestern Peru: Cretaceous-Tertiary total petroleum system. US Geol. Surv. Bull. 2206-A, 1–20. https://doi.org/10.3133/b2206A.
Hodgson, D.M., Peakall, J., Maier, K.L., 2022. Submarine channel mouth settings: Processes, geomorphology, and deposits. Front. Earth Sci. 10, 790320. https://doi.org/10.3389/feart.2022.790320.
Jackson, C.A.L., Larsen, E., Hanslien, S., Tjemsland, A., 2011. Controls on synrift turbidite deposition on the hanging wall of the South Viking Graben, North Sea rift system, offshore Norway. AAPG Bull. 95, 1557–1587. https://doi.org/10.1306/01031110037.
Jiang, Z., 2018. Sedimentary Dynamics of windfield-source-basin System: New Concept for Interpretation and Prediction. Springer, Beijing, pp. 57–63.
Jin, M., Tan, X., Tong, M., Zeng, W., Liu, H., Zhong, B., Liu, Q., Lian, C., Zhou, X., Xu, H., Luo, B., 2017. Karst paleogeomorphology of the fourth member of Sinian Dengying formation in Gaoshiti-Moxi area, Sichuan Basin, SW China: Restoration and geological significance. Petrol. Explor. Dev. 44, 58–68. https://doi.org/10.1016/S1876-3804(17)30008-3.
Kane, I.A., Kneller, B.C., Dykstra, M., Kassem, A., McCaffrey, W.D., 2007. Anatomy of a submarine channel-levee: An example from Upper Cretaceous slope sediments, Rosario Formation, Baja California, Mexico. Mar. Petrol. Geol. 24, 540–563. https://doi.org/10.1016/j.marpetgeo.2007.01.003.
Kneller, B., 1995. Beyond the turbidite paradigm: Physical models for deposition of turbidites and their implications for reservoir prediction. In: Hartley, A.J., Prosser, D.J. (Eds.), Characterization of deep marine clastic systems. Geological Society, London, Special Publications, pp. 31–49. https://doi.org/10.1144/GSL.SP.1995.094.01.04.
Leeder, M.R., Gawthorpe, R.L., 1987. Sedimentary models for extensional tilt-block/half-graben basins. In: Coward, M.P., Dewey, J.F., Hancock, P.L. (Eds.), continental extensional tectonics. Geological Society, London, Special Publications, pp. 139–152. https://doi.org/10.1144/GSL.SP.1987.028.01.11.
Li, S., Li, S., Shan, X., Gong, C., Yu, X., 2017. Classification, formation, and transport mechanisms of mud clasts. Int. Geol. Rev. 59, 1609–1620. https://doi.org/10.1080/00206814.2017.1287014.
Li, W., Yue, D., Wu, S.H., Wang, W.F., Li, J., Wang, W.R., Tian, T.H., 2019. Characterizing meander belts and point bars in fluvial reservoirs by combining spectral decomposition and genetic inversion. Mar. Petrol. Geol. 105, 168–184. https://doi.org/10.1016/j.marpetgeo.2019.04.015.
Lin, P., Wu, S.H., Zhang, J.J., Hu, G.Y., Xia, Q.Y., Fan, H.J., Wang, N.S., 2018. Distribution of submarine fans in the thrust fault zone of continental slope, Niger Delta Basin. Oil Gas Geol. 39, 1073–1086. https://doi.org/10.11743/ogg20180521 (in Chinese).
Lin, Y., Wu, S.H., Wang, X., Zhao, X.M., Ling, Y., Lu, Y., Zhang, J.J., 2014. Research on reservoir architecture models of deep-water turbidite lobes. Nat. Gas Geosci. 25 (8), 1197–1204. https://doi.org/10.11764/j.issn.1672-1926.2014.08.1197 (in Chinese).
Liu, M.C., Wu, S.H., Yue, D.L., Xu, Z.H., Wan, X.L., Wu, H.L., Chen, Z.H., Li, Z., 2025. Palaeogeomorphological control on the depositional architecture of lacustrine gravity-flow deposits in a depression lacustrine basin: A case study of the Triassic Yanchang Formation, southern Ordos Basin, China. J. Palaeogeogr. 14 (2), 476–500. https://doi.org/10.1016/j.jop.2025.01.003.
Lowe, D.R., LoPiccolo, R.D., 1974. The characteristics and origins of dish and pillar structures. J. Sediment. Res. 44, 483–501. https://doi.org/10.1306/74D72A68-2B21-11D7-8648000102C1865D.
Lowe, D.R., 1982. Sediment gravity flows; II, depositional models with special reference to the deposits of high-density turbidity currents. J. Sediment. Res. 52, 279–297. https://doi.org/10.1306/212F7F31-2B24-11D7-8648000102C1865D.
Lyu, Q.Q., Fu, J.H., Luo, S.H., Li, S.X., Zhou, X.P., Pu, Y.X., Yan, H.G., 2022. Sedimentary characteristics and model of gravity flow channel-lobe complex in a depression lake basin: A case study of Chang 7 Member of Triassic Yanchang Formation in Southwestern Ordos Basin, NW China. Petrol. Explor. Dev. 49, 1323–1338. https://doi.org/10.1016/S1876-3804(23)60352-0.
McArthur, A.D., Hartley, A.J., Archer, S.G., Jolley, D.W., Lawrence, H.M., 2016. Spatiotemporal relationships of deep-marine, axial, and transverse depositional systems from the synrift Upper Jurassic of the central North Sea. AAPG Bull. 100, 1469–1500. https://doi.org/10.1306/04041615125.
McHargue, T.R., Hodgson, D.M., Shelef, E., 2021. Architectural diversity of submarine lobate deposits. Front. Earth Sci. 9, 1–21. https://doi.org/10.3389/feart.2021.697170.
McHargue, T., Pyrcz, M.J., Sullivan, M.D., Clark, J.D., Fildani, A., Romans, B.W., Covault, J.A., Levy, M., Posamentier, H.W., Drinkwater, N.J., 2011. Architecture of turbidite channel systems on the continental slope: Patterns and predictions. Mar. Petrol. Geol. 28, 728–743. https://doi.org/10.1016/j.marpetgeo.2010.07.008.
McKinnon, M., 2013. Depositional character of “Syn-Rift,” deep-water deposits: A case study from the Upper Jurassic buzzard turbidite system. University of Aberdeen.
Moody, J.D., Pyles, D.R., Clark, J., Bouroullec, R., 2012. Quantitative outcrop characterization of an analog to weakly confined submarine channel systems: Morillo 1 member, Ainsa Basin, Spain. AAPG Bull. 96, 1813–1841. https://doi.org/10.1306/01061211072.
Mutti, E., Normark, W.R., 1987. Comparing examples of modern and ancient turbidite systems: problems and concepts. In: Leggett, J.K., Zuffa, G.G. (Eds.), Marine Clastic Sedimentology: Concepts and Case Studies. Graham and Troutman, London, pp. 1–38.
Mutti, E., 1977. Distinctive thin-bedded turbidite facies and related depositional environments in the Eocene Hecho Group (South-central Pyrenees, Spain). Sedimentology 24, 107–131. https://doi.org/10.1111/j.1365-3091.1977.tb00122.x.
Normark, W.R., 1970. Growth patterns of deep-sea fans. AAPG Bull. 54 (11), 2170–2195. https://doi.org/10.1306/5D25CC79-16C1-11D7-8645000102C1865D.
Normark, W.R., Piper, D.J.W., Hiscott, R.N., 1998. Sea level controls on the textural characteristics and depositional architecture of the Hueneme and associated submarine fan systems, Santa Monica Basin, California. Sedimentology 45, 53–70. https://doi.org/10.1046/j.1365-3091.1998.00139.x.
Nyíri, D., Tőkés, L., Zadravecz, C., Fodor, L., 2021. Early post-rift confined turbidite systems in a supra-detachment basin: implications for the early to middle Miocene basin evolution and hydrocarbon exploration of the Pannonian Basin. Global Planet. Change 203, 103500. https://doi.org/10.1016/j.gloplacha.2021.103500.
Partington, M.A., Mitchener, B.C., Milton, N.J., Fraser, A.J., 1993. Genetic sequence stratigraphy for the North Sea Late Jurassic and Early Cretaceous; distribution and prediction of Kimmeridgian-late Ryazanian reservoirs in the North Sea and adjacent areas, Petroleum Geology of Northwest Europe. In: Proceedings of the 4th Conference. London, pp. 347–370. https://doi.org/10.1144/0040347.
Patruno, S., Kombrink, H., Archer, S.G., 2021. Cross-Border Stratigraphy of the Northern, Central and Southern North Sea: A Comparative Tectono-Stratigraphic Megasequence Synthesis. Geological Society, London, Special Publications, pp. 13–83. https://doi.org/10.1144/SP494-2020-228.
Picot, M., Droz, L., Marsset, T., Dennielou, B., Bez, M., 2016. Controls on turbidite sedimentation: insights from a quantitative approach of submarine channel and lobe architecture (Late Quaternary Congo Fan). Mar. Petrol. Geol. 72, 423–446. https://doi.org/10.1016/j.marpetgeo.2016.02.004.
Pohl, F., 2019. Turbidity currents and their deposits in abrupt morphological transition zones. Utrecht University.
Pohl, F., Eggenhuisen, J.T., Cartigny, M.J.B., Tilston, M.C., de Leeuw, J., Hermidas, N., 2020. The influence of a slope break on turbidite deposits: An experimental investigation. Mar. Geol. 424, 106160. https://doi.org/10.1016/j.margeo.2020.106160.
Posamentier, H.W., Walker, R.G., 2006. Deep-water turbidites and submarine fans. In: Posamentier, H.W., Walker, R.G. (Eds.), Facies Models Revisited, vol. 84. SEPM Special Publications, pp. 399–520.

Postma, G., Cartigny, M.J.B., 2014. Supercritical and subcritical turbidity currents and their deposits; a synthesis. Geology 42, 987–990. https://doi.org/10.1130/G35957.1.
Postma, G., Cartigny, M.J.B., Kleverlaan, K., 2009. Structureless, coarse-tail graded Bouma Ta formed by internal hydraulic jump of the turbidity current? Sediment. Geol. 219 (1–4), 1–6. https://doi.org/10.1016/j.sedgeo.2009.05.018.
Postma, G., Kleverlaan, K., Cartigny, M.J.B., 2014. Recognition of cyclic steps in sandy and gravelly turbidite sequences, and consequences for the Bouma facies model. Sedimentology 61, 2268–2290. https://doi.org/10.1111/sed.12135.
Prélat, A., Hodgson, D.M., Flint, S.S., 2009. Evolution, architecture and hierarchy of distributary deep-water deposits: a high-resolution outcrop investigation from the Permian Karoo Basin, South Africa. Sedimentology 56, 2132–2154. https://doi.org/10.1111/j.1365-3091.2009.01073.x.
Privat, A.M.L.J., Peakall, J., Hodgson, D.M., Schwarz, E., Jackson, C.A.L., Arnol, J.A., 2024. Evolving fill-and-spill patterns across linked early post-rift depocentres control lobe characteristics: Los Molles Formation, Argentina. Sedimentology 71, 1639–1685. https://doi.org/10.1111/sed.13190.
Prosser, S., 1993. Rift-related linked depositional systems and their seismic expression. In: Williams, G.D., Dobb, A. (Eds.), Tectonics and Seismic Sequence Stratigraphy, vol. 71. Geological Society, London, Special Publications, pp. 35–66. https://doi.org/10.1144/GSL.SP.1993.071.01.03.
Ravnas, R., Steel, R.J., 1998. Architecture of marine rift-basin successions. AAPG Bull. 82, 110–146. https://doi.org/10.1306/1D9BC3A9-172D-11D7-8645000102C1865D.
Ray, F.M., Pinnock, S.J., Katamish, H., Turnbull, J.B., 2010. The buzzard field: anatomy of the reservoir from appraisal to production. In: Petroleum Geology: From Mature Basins to New Frontiers – Proceedings of the 7th Petroleum Geology Conference. Geological Society, London, pp. 369–386. https://doi.org/10.1144/0070369.
Richards, M., Bowman, M., Reading, H., 1998. Submarine-fan systems; I, Characterization and stratigraphic prediction. Mar. Petrol. Geol. 15, 689–717. https://doi.org/10.1016/S0264-8172(98)00036-1.
Sclater, J.G., Christie, P.A.F., 1980. Continental stretching: an explanation of the post-mid-cretaceous subsidence of the central North Sea Basin. J. Geophys. Res. 85 (B7), 3711–3739. https://doi.org/10.1029/JB085iB07p03711.
Shanmugam, G., Moiola, R.J., 1988. Submarine fans; characteristics, models, classification, and reservoir potential. Earth Sci. Rev. 24, 383–428. https://doi.org/10.1016/0012-8252(88)90064-5.
Shanmugam, G., 1996. High-density turbidity currents; are they sandy debris flows? J. Sediment. Res. 66, 2–10. https://doi.org/10.1306/D426828E-2B26-11D7-8648000102C1865D.
Shanmugam, G., 1997. The bouma sequence and the turbidite mind set. Earth Sci. Rev. 42 (4), 201–229. https://doi.org/10.1016/S0012-8252(97)81858-2.
Shanmugam, G., 2016. Submarine fans: A critical retrospective (1950–2015). J. Palaeogeogr. 5, 110–184. https://doi.org/10.1016/j.jop.2015.08.011.
Shanmugam, G., Damuth, J.E., Moiola, R.J., 1985. Is the turbidite facies association scheme valid for interpreting ancient submarine fan environments? Geology 13, 234–237. https://doi.org/10.1130/0091-7613(1985)13<234:ITFAS>2.0.CO;2.
Shanmugam, G., Lehtonen, L.R., Straume, T., Syvertsen, S.E., Hodgkinson, R.J.S.M., 1994. Slump and debris-flow dominated upper slope facies in the Cretaceous of the Norwegian and Northern North seas (61 – 67°N): Implications for sand Distribution1. AAPG Bull. 6, 910–937. https://doi.org/10.1306/A25FE3E7-171B-11D7-8645000102C1865D.
Sharp, I.R., Gawthorpe, R.L., Armstrong, B., Underhill, J.R., 2000. Propagation history and passive rotation of mesoscale normal faults: Implications for synrift stratigraphic development. Basin Res. 12, 285–305. https://doi.org/10.1111/j.1365-2117.2000.00132.x.
Stevenson, C.J., Jackson, C.A., Hodgson, D.M., Hubbard, S.M., Eggenhuisen, J.T., 2015. Deep-water sediment bypass. J. Sediment. Res. 85, 1058–1081. https://doi.org/10.2110/jsr.2015.63.
Steventon, M.J., Jackson, C.A.L., Johnson, H.D., Hodgson, D.M., Kelly, S., Omma, J., Gopon, C., Stevenson, C., Fitch, P., 2021. Evolution of a sand-rich submarine channel–lobe system, and the impact of mass-transport and transitional-flow deposits on reservoir heterogeneity: Magnus field, Northern North Sea. Pet. Geosci. 27, 2020–2095. https://doi.org/10.1144/petgeo2020-095.
Stow, D.A.V.A., Howell, D.G., Nelson, C.H., 1984. Sedimentary, tectonic, and sea-level controls on submarine fan and slope-apron turbidite systems. Geo Mar. Lett. 3, 57–64. https://doi.org/10.1007/BF02462448.
Sullivan, M.D., Jensen, G.N., Goulding, F.J., Jennette, D.C., Foreman, J.L., Stern, D., 2000. Architectural analysis of deep-water outcrops: Implications for exploration and production of the Diana Sub-basin, Western Gulf of Mexico. In: Weimer, P., Slatt, R.M., Coleman, J., Rosen, N.C., Nelson, H., Bouma, A.H., Styzen, M.J., Lawrence, D.T. (Eds.), Deep-Water Reservoirs of the World. Gulf Coast Section SEPM 20th Bob F. Perkins Research Conference, pp. 1010–1032.
Tang, Y., Chai, H., Wang, H., Zhang, L., Chen, P., Luo, M., Zhang, W., Jiang, L., Pan, X., Wang, C., Shan, Y., 2023. Seismic geomorphology analysis and petroleum geology significance of presalt Jurassic carbonate in the right bank of Amu Darya River. Geoenergy Sci. Eng. 230. https://doi.org/10.1016/j.geoen.2023.212266.
Taylor, E.E., Webb, N.J., Stevenson, C.J., Henderson, J.R., Kovac, A., Millington, J.J., Rhodes, J.A., 2020. The buzzard field, blocks 19/5a, 19/10a, 20/1 and 20/6a, UK North Sea. In: Goffey, G., Gluyas, J.G. (Eds.), United Kingdom Oil and Gas Fields: 50Th Anniversary Commemorative Volume. Geological Society, London, Memoirs, pp. 17–33. https://doi.org/10.1144/M52.
Tian, D., Liang, C., Jiang, T., Pei, J., Liao, J., 2024. Architecture and depositional processes of a submarine channel during the late Miocene in the Yinggehai Basin, northwestern South China Sea. Mar. Petrol. Geol. 167, 106964. https://doi.org/10.1016/j.marpetgeo.2024.106964.
Tian, R., Xian, B., Wu, Q., Shu, Q., Liu, J., Zhang, W., Wang, Z., Li, Q., Rahman, N.U., Gao, Y., Wang, J., 2023. Turbidite system controlled by fault interaction and linkage on a slope belt of rift basin: Zhanhua depression, Bohai Bay Basin, China. Mar. Petrol. Geol. 155, 106377. https://doi.org/10.1016/j.marpetgeo.2023.106377.
Tillmans, F., Gawthorpe, R.L., Jackson, C.A.L., Rotevatn, A., 2021. Syn-rift sediment gravity flow deposition on a late Jurassic fault-terraced slope, northern North Sea. Basin Res. 33, 1844–1879. https://doi.org/10.1111/bre.12538.
Underhill, J.R., Richardson, N., 2022. Geological controls on petroleum plays and future opportunities in the North Sea Rift Super Basin. AAPG Bull. 106, 573–631. https://doi.org/10.1306/07132120084.
Underhill, L.R., 1998. Jurassic. In: Glennie, K.W. (Ed.), Petroleum Geology of the North Sea: Basic Concepts and Recent Advances, fourth ed., pp. 245–293.
Ventra, D., Cartigny, M.J.B., Bijkerk, J.F., Acikalin, S., 2015. Supercritical-flow structures on a late carboniferous delta front: Sedimentologic and paleoclimatic significance. Geology 43 (8), G36708.1. https://doi.org/10.1130/G36708.1.
Wang, Y.M., Liu, H., Li, L.C., Qi, X.F., Wang, Y., 2002. Types and distribution characteristics of slope breaks of large-type down-warped lake basins. Earth Sci. J. China Univ. Geosci. 27 (6), 683–688. https://doi.org/10.3321/j.issn:1000-2383.2002.06.005 (in Chinese).
Weimer, P., Link, M.H., 1991. Global petroleum occurrences in submarine fans and turbidite systems. In: Weimer, P., Link, M.H. (Eds.), Seismic Facies and Sedimentary Processes of Submarine Fans and Turbidite Systems. Springer Verlag, New York, pp. 9–67.
Yu, T., Liu, H., Liu, B., Tang, S., Tang, Y., Yin, C., 2022. Restoration of karst paleogeomorphology and its significance in petroleum geology-using the top of the Middle Triassic Leikoupo formation in the northwestern Sichuan Basin as an example. J. Petrol. Sci. Eng. 208, 109638. https://doi.org/10.1016/j.petrol.2021.109638.
Zakaria, A.A., Johnson, H.D., Jackson, C.A.L., Tongkul, F., 2013. Sedimentary facies analysis and depositional model of the Palaeogene West Crocker submarine fan system, NW Borneo. J. Asian Earth Sci. 76, 283–300. https://doi.org/10.1016/j.jseaes.2013.05.002.
Zhang, J.J., Wu, S.H., Fan, T.E., Fan, H.J., Jiang, L., Chen, C., Wu, Q.Y., Lin, P., 2016. Research on the architecture of submarine-fan lobes in the Niger Delta Basin, offshore West Africa. J. Palaeogeogr. 5, 185–204. https://doi.org/10.1016/j.jop.2016.05.005.
Zhang, J.J., Wu, S.H., Hu, G.Y., Fan, T.E., Yu, B., Lin, P., Jiang, S.H., 2018. Sea-level control on the submarine fan architecture in a deepwater sequence of the Niger Delta Basin. Mar. Petrol. Geol. 94, 179–197. https://doi.org/10.1016/j.marpetgeo.2018.04.002.
Zhang, J.J., Wu, S.H., Wang, X., Lin, Y., Fan, H.J., Jiang, L., Wan, Q.H., Yin, H., Lu, Y., 2015. Reservoir quality variations within a sinuous deep water channel system in the Niger Delta Basin, offshore West Africa. Mar. Petrol. Geol. 63, 166–188. https://doi.org/10.1016/j.marpetgeo.2015.02.041.